



February 27, 2021

We present an original manuscript entitled “A Reduced Order Approach for Probabilistic Inversions of 3D Magnetotelluric Data II: Joint inversion of MT and Surface-Wave Data” by M.C. Manassero¹, J. C. Afonso^{1,2}, F. Zyserman³, S. Zlotnik⁴ and I. Fomin¹.

This paper is a non-peer reviewed preprint submitted to EarthArXiv. The preprint was submitted for peer review to Journal of Geophysical Research: Solid Earth on February 27, 2021 (awaiting for reviews).

Yours Sincerely,

Maria Constanza Manassero*
Juan Carlos Afonso,
Fabio Zyserman,
Sergio Zlotnik,
Ilya Fomin

¹ Australian Research Council Centre of Excellence for Core to Crust Fluid Systems/GEMOC, Department of Earth and Environmental Sciences, Macquarie University. (maria-constanza.manassero@mq.edu.au, juan.afonso@mq.edu.au, ilya.fomin@mq.edu.au)

² Centre for Earth Evolution and Dynamics, Department of Geosciences, University of Oslo, Norway.

³ CONICET, ; Universidad Nacional de La Plata, Facultad de Ciencias Astronomicas y Geofisicas (zyserman@fcaglp.unlp.edu.ar).

⁴ Laboratori de C`alcul Num`eric, Escola T`ecnica Superior d`Enginyers de Camins, Canals i Ports, Universitat Polit`ecnica de Catalunya, Barcelona, Spain. (sergio.zlotnik@upc.edu)

*Corresponding author

Australian Research Council Centre of Excellence for Core to Crust Fluid System (CCFS)

Department of Earth and Environmental Sciences, Macquarie University, Sydney, NSW 2109 , Australia

email: maria-constanza.manassero@mq.edu.au

A Reduced Order Approach for Probabilistic Inversions of 3D Magnetotelluric Data II: Joint inversion of MT and Surface-Wave Data

M.C. Manassero¹, J.C. Afonso^{1,2}, F. Zyserman³, S. Zlotnik⁴ and I. Fomin¹

¹Australian Research Council Centre of Excellence for Core to Crust Fluid Systems/GEMOC,

Department of Earth and Environmental Sciences, Macquarie University, Sydney, Australia.

²Centre for Earth Evolution and Dynamics, Department of Geosciences, University of Oslo, Norway.

³CONICET, Facultad de Ciencias Astronómicas y Geofísicas, Universidad de La Plata, Argentina.

⁴Laboratori de Càlcul Numèric, Escola Tècnica Superior d'Enginyers de Camins, Canals i Ports,

Universitat Politècnica de Catalunya, Barcelona, Spain.

Key Points:

- We present a novel strategy to invert 3D magnetotelluric (MT) data together with other data sets in a fully probabilistic manner.
- We apply our method and perform the first joint probabilistic inversions of 3D MT and surface-wave dispersion data for imaging the electrical conductivity distribution in the lithosphere.
- We demonstrate the capability and applicability of our approach to include 3D MT data into joint probabilistic inversions for the physical state of the interior of the Earth.

Corresponding author: Maria Constanza Manassero, maria-constanza.manassero@mq.edu.au

Abstract

Joint probabilistic inversions of magnetotelluric (MT) and seismic data has great potential for imaging the thermochemical structure of the lithosphere as well as mapping fluid/melt pathways and regions of mantle metasomatism. In this contribution we present a novel probabilistic (Bayesian) joint inversion scheme for 3D MT and surface-wave dispersion data particularly designed for large-scale lithospheric studies. The approach makes use of a recently developed strategy for fast solutions of the 3D MT forward problem (Manassero et al., 2020) and combines it with adaptive Markov chain Monte Carlo (MCMC) algorithms and parallel-in-parallel strategies to achieve extremely efficient simulations. To demonstrate the feasibility, benefits and performance of our joint inversion method to image the conductivity, temperature and velocity structures of the lithosphere, we apply it to two numerical examples of increasing complexity. The inversion approach presented here is timely and will be useful in the joint analysis of MT and surface wave data that are being collected in many parts of the world. This approach also opens up new avenues for the study of translithospheric and transcrustal magmatic systems, the detection of metasomatised mantle and the incorporation of MT into multi-observable inversions for the physical state of the Earth’s interior.

1 Introduction

Joint inversions of two or more geophysical data sets are common practice for imaging the Earth’s interior and elucidating the physical state of the planet. When the inverted data sets have complementary sensitivities to the properties of interest, joint inversions can significantly reduce the ambiguity inherent in single-dataset inversions, achieve more stable solutions, increase identifiability of features and enhance model resolution. Perhaps more importantly, certain properties of the Earth’s interior can only be revealed by combining observations from different techniques. An example is the bulk composition of the lithospheric mantle, which requires independent constraints on the bulk density (e.g. from gravity data sets) and shear-wave velocity (e.g. from surface-wave data). Recent discussions on the benefits and limitations of joint approaches for imaging the structure of the lithosphere and upper mantle can be found in e.g. Khan et al. (2006); J. Afonso et al. (2013a); J. C. Afonso, Moorkamp, & Fullea (2016) and Moorkamp (2017). The joint inversion of magnetotelluric (MT) with seismic data (e.g. Khan et al., 2006; Moorkamp et al., 2007; Gallardo & Meju, 2007; Jegen et al., 2009; Moorkamp et al., 2010; Vozar et al., 2014; Bennington et al., 2015; J. C. Afonso, Rawlinson, et al., 2016; Jones et al., 2017) is of particular interest as they offer complementary sensitivities to temperature, composition and fluid/melt content that are impossible to obtain with other data sets (e.g. Gallardo & Meju, 2007; Moorkamp et al., 2007; Jones et al., 2009; Moorkamp et al., 2010; Selway et al., 2019; J. C. Afonso, Rawlinson, et al., 2016; J. C. Afonso, Moorkamp, & Fullea, 2016). In the context of whole-lithosphere structure, both seismic (or seismic + gravity) and MT data can be used to put constraints on the background (or regional) thermal and mineralogical structure (e.g. Jones et al., 2009; S.-i. Karato & Wang, 2013; J. C. Afonso, Rawlinson, et al., 2016; J. C. Afonso, Moorkamp, & Fullea, 2016), but only MT is strongly sensitive to hydrogen content, minor conductive phases and/or small volumes of fluid or melt (S.-I. Karato, 1990; S.-i. Karato, 2006; R. Evans, 2012; Yoshino, 2010; Khan, 2016; Selway, 2014). Therefore, while both data sets should converge towards a consistent view of the background thermochemical structure, they will diverge towards regions where the electrical conductivity of rocks is affected by factors other than temperature or bulk composition. This makes MT-seismic joint inversions a powerful means to detect fluid pathways in the lithosphere, (e.g. Selway & O’Donnell, 2019; R. L. Evans et al., 2019), including the locus of partial melting, ore deposits and hydrated (or metasomatized) lithologies. This unique potential of joint MT-seismic inversions has also given impetus to the acquisition of collocated MT and seismic data over large regions. Concrete examples are the MAGIC and EarthScope USArray in USA (www.usarray.org), the AusLAMP program and AusArray in Australia (www.ga.gov.au/efft/minerals/nawa),

73 the IberArray (www.iberarray.ictja.csic.es/) in Europe and the Sinoprobe in China (www.sinoprobe.org).
 74 These programs are providing high-quality seismic and MT data with unprecedented res-
 75 olution and coverage, allowing the pursue of large-scale 3D joint inversions for the phys-
 76 ical state of the whole lithosphere and upper mantle.

77 The actual approach to the joint inversion of MT with seismic data is still a mat-
 78 ter of much debate. While traditional deterministic methods are computationally effi-
 79 cient, they are not well prepared to deal with the inherent non-uniqueness of geophys-
 80 ical data sets, and MT data in particular (e.g. Wait, 1962; Parker, 1971; Oldenburg, 1979;
 81 Mallick & Verma, 1979; Parker, 1980). They are also generally unstable with respect to
 82 measurement and/or modeling errors (thus requiring strong regularization) and ill-suited
 83 for global uncertainty analysis (e.g. J. C. Afonso, Moorkamp, & Fulla, 2016; Moorkamp,
 84 2017). Probabilistic inversion methods represent an attractive alternative (Tarantola,
 85 2005; Gregory, 2005; Mosegaard & Hansen, 2016) as they are less susceptible to the above-
 86 mentioned limitations and provide substantially more information on the parameters of
 87 interest via full probability distributions. In probabilistic or Bayesian approaches, the
 88 solution to the inverse problem is given by the so-called posterior probability density dis-
 89 tribution (PDF) over the model parameter space. This PDF summarizes all the infor-
 90 mation about the unknown parameters and their uncertainties conditioned on the data
 91 and modeling assumptions. As such, it represents the most general solution to the in-
 92 verse problem. In high-dimensional and/or non-linear problems with complex priors, the
 93 posterior PDF cannot be represented analytically and it needs to be sampled point-wise
 94 using e.g. Markov chain Monte Carlo (MCMC) algorithms (Mosegaard & Tarantola, 1995;
 95 Gilks et al., 1995; Tarantola, 2005; Gregory, 2005). This particular sampling-based ap-
 96 proach to probabilistic inversions makes them less efficient than deterministic approaches,
 97 as they typically require the numerical solution of millions of forward problems. When
 98 the forward problems are computationally expensive, probabilistic approaches can be ren-
 99 dered impractical.

100 Joint probabilistic inversions of MT and seismic data have been successfully im-
 101 plemented by e.g. Khan et al. (2006, 2008); J. Afonso et al. (2013a); J. C. Afonso et al.
 102 (2013b); Vozar et al. (2014) and Jones et al. (2017) in the context of 1D MT data only.
 103 For the cases of 2D and 3D MT data, however, the large computational cost of the MT
 104 forward problem has been the main impediment for pursuing probabilistic inversions,
 105 as the number of forward solutions required are typically on the order of $10^5 - 10^7$.

106 In recent years, various methods and strategies for reducing the cost of full forward
 107 solutions have been proposed (see reviews in Frangos et al., 2011; Peherstorfer et al., 2018).
 108 The general idea behind these methods is the construction of an approximation, called
 109 the *low-fidelity* or *surrogate* model, which can be used instead of, or combined with, the
 110 costly full forward or *high-fidelity* solution. Having a faster surrogate of the forward prob-
 111 lem is beneficial in a number of contexts, but it is particularly attractive in the context
 112 of MCMC schemes used to estimate the posterior PDF in a probabilistic inversion (Chris-
 113 ten & Fox, 2005; Cui et al., 2015; Florentin & Díez, 2012; Conrad et al., 2016; Galabert
 114 et al., 2019; Manassero et al., 2020; J. Zhang & Taflanidis, 2019). In traditional imple-
 115 mentations, the surrogates are computed in an *offline* stage (prior to the probabilistic
 116 inversion) at specific locations within the parameter space called ‘snapshots’. However,
 117 it has been recently shown (Cui et al., 2015; Yan & Zhou, 2019; J. Zhang & Taflanidis,
 118 2019; Galabert et al., 2019; Manassero et al., 2020) that in the context of high- and ultra-
 119 high-dimensional probabilistic inversions, it is practically impossible to pre-explore the
 120 parameter space in an offline stage to create surrogates that will guarantee accurate so-
 121 lutions within the so far unknown high-probability regions. In these situations, an adap-
 122 tive MCMC approach where the surrogate is refined *online* during the MCMC simula-
 123 tion is a more effective and efficient approach. A strategy to reduce the computational
 124 cost of the 3D MT forward solver and perform full probabilistic 3D MT inversions has
 125 recently been presented by Manassero et al. (2020). This novel strategy, called RB+MCMC,

126 combines i) an efficient parallel-in-parallel structure to solve the 3D MT forward prob-
 127 lem, ii) a Reduced Basis Method to create fast and accurate surrogate models of the *high-*
 128 *fidelity* solution, and iii) adaptive strategies for both the MCMC algorithm and the sur-
 129rogate model.

130 This paper builds on our previous work (Manassero et al., 2020) and presents the
 131 first joint inversion of 3D magnetotelluric and surface-wave data within the context of
 132 MCMC-driven, fully probabilistic inversions. Specifically, we focus on a realistic 3D map-
 133 ping of the electrical conductivity structure of the lithosphere including the locus of deep
 134 thermochemical anomalies and fluid pathways. We adopt the RB+MCMC strategy to
 135 compute 3D MT surrogate models and propose complementary parameterizations to cou-
 136 ple both data sets. Using realistic, whole-lithosphere synthetic models, we demonstrate
 137 the benefits and general capabilities of our method for 3D joint probabilistic inversions
 138 of MT with surface-wave data in particular, and with other data sets in general.

139 2 Bayesian Inversion

Within the context of Bayesian inference, the most general solution to the inverse
 problem is represented by a multi-dimensional probability density function (PDF) over
 the combined parameter-data space (cf. Tarantola & Valette, 1982; Gilks et al., 1995;
 Mosegaard et al., 2002; Gregory, 2005; Kaipio & Somersalo, 2006; Mosegaard & Hansen,
 2016). This distribution is known as the *posterior* PDF and can be thought of as an ob-
 jective measure of our best state of knowledge on the problem at hand. It is obtained
 as a conjunction of the available information on the model parameters (\mathbf{m}), the data (\mathbf{d}),
 and their uncertainties. In particular, the marginal posterior PDF over the model pa-
 rameters, $P(\mathbf{m}|\mathbf{d})$, is formally given by

$$P(\mathbf{m}|\mathbf{d}) \propto \mathcal{L}(\mathbf{m})P(\mathbf{m}). \quad (1)$$

140 where $P(\mathbf{m})$ is a PDF encoding *a priori* information on the parameter space (what we
 141 know or believe about the unknown model parameters prior to considering the actual
 142 data) and $\mathcal{L}(\mathbf{m})$ is the so-called *likelihood* function, which describes the probability of
 143 obtaining the observed data \mathbf{d} given \mathbf{m} . In general, $P(\mathbf{m}|\mathbf{d})$ will be non-linear and high-
 144 dimensional (and possibly multi-peaked), with no simple analytical description. When
 145 this is the case, unbiased approximations of $P(\mathbf{m}|\mathbf{d})$ are commonly obtained via Markov
 146 chain Monte Carlo (MCMC) methods (Gilks et al., 1995; Mosegaard & Tarantola, 1995;
 147 Tarantola, 2005; Gregory, 2005). These type of algorithms are designed to output Markov
 148 chains that have $P(\mathbf{m}|\mathbf{d})$ as their equilibrium distributions by repeatedly drawing mod-
 149 els \mathbf{m}_t and evaluating their posterior probability $P(\mathbf{m}_t|\mathbf{d})$. A large number of MCMC
 150 methods have been proposed in the literature, all with relative merits and drawbacks.
 151 We refer the reader to the excellent monographs by e.g. Tarantola & Valette (1982); Gilks
 152 et al. (1995); Gregory (2005); Calvetti & Somersalo (2007) and Mosegaard & Hansen (2016)
 153 for in-depth treatments of Bayesian and MCMC methods applied to inverse problems.
 154 In the following, we restrict ourselves to describing only the most relevant theoretical
 155 and computational aspects for our purposes.

156 2.1 The Likelihood Function

The construction of an appropriate likelihood function $\mathcal{L}(\mathbf{m})$ is a critical part of
 any Bayesian inference problem. $\mathcal{L}(\mathbf{m})$ is typically specified by the distribution of the
 data uncertainty, which includes both observational and modelization errors. In most
 cases, observational errors are relatively straightforward to model. Modelization errors,
 on the other hand, are more complex (and commonly ignored in most geophysical stud-
 ies) to describe and typically involves exploratory assessments of both numerical errors
 - e.g. convergence analyses - and Monte Carlo estimates of the correlations between dif-
 ferent data sets (see discussions and approaches in Gouveia & Scales, 1998; J. Afonso

et al., 2013a). In the convenient (and most popular) case where both observational and modelization errors can be assumed to be approximately Gaussian, the likelihood function takes the form:

$$\mathcal{L}(\mathbf{m}) \propto \left(-\frac{1}{2}(\mathbf{g}(\mathbf{m}) - \mathbf{d})^t(\mathbf{C}_d + \mathbf{C}_T)^{-1}(\mathbf{g}(\mathbf{m}) - \mathbf{d})^t \right), \quad (2)$$

157 where \mathbf{C}_d and \mathbf{C}_T are the covariance matrices representing the data and theoretical (model)
 158 uncertainties, respectively, and $\mathbf{g}(\mathbf{m})$ denotes the data predicted by the *forward prob-*
 159 *lem* for model \mathbf{m} . The term within the parenthesis in Eq. 2 is commonly referred to as
 160 the *misfit* of model \mathbf{m} .

In the case of joint inversions of uncorrelated observational data sets, the likelihood function can be written as the product of partial likelihoods:

$$\mathcal{L}(\mathbf{m}) = \prod \mathcal{L}_j(\mathbf{m}), \quad (3)$$

161 where \mathcal{L}_j refers to the likelihood associated with the dataset \mathbf{d}^j . The assumption of in-
 162 dependent observational data is well justified in most practical situations, an in partic-
 163 ular in the MT+seismic case discussed in this paper, as different data sets are commonly
 164 gathered in separate surveys using different instrumentation. An important practical ad-
 165 vantage of the factorization of the likelihood into partial likelihoods (Eq. 3) is that it makes
 166 it possible to adopt a Cascaded Metropolis (CM) approach (Tarantola, 2005; B. Hassani
 167 & Renaudin, 2013), which is typically more efficient than a standard Metropolis-Hastings
 168 algorithm applied to the total likelihood.

169 2.2 Cascaded-Metropolis Algorithm

170 The CM algorithm is particularly useful when the different data sets jointly inverted
 171 are uncorrelated, have complementary sensitivities to different aspects of the problem,
 172 and at least one of the forward solvers is more computationally demanding than the oth-
 173 ers. The basic idea is to apply a Metropolis criterion sequentially to each partial pos-
 174 terior (prior \times partial likelihood), which becomes an updated prior in the evaluation of
 175 the subsequent partial posterior (e.g. B. Hassani & Renaudin, 2013; B. K. Hassani & Re-
 176 naudin, 2018). The practical benefits of the above procedure are significant when the
 177 partial likelihoods are arranged in order of computational complexity or cost, as there
 178 is no need to compute expensive forwards for models that are rejected early in the se-
 179 quence (see e.g. Tarantola, 2005, for further details).

The basic procedure for the case of two forward operators is as follows: For a new sample \mathbf{m}_t , the first partial posterior $P_1(\mathbf{m}_t|\mathbf{d}) = \mathcal{L}_1(\mathbf{m}_t)P(\mathbf{m})$ is always computed using the computationally inexpensive forward. If $P_1(\mathbf{m}_t|\mathbf{d}) > P_1(\mathbf{m}_{t-1}|\mathbf{d})$, this first posterior becomes a prior in the evaluation of the second partial posterior which is now obtained from the expensive forward:

$$P_2(\mathbf{m}_t|\mathbf{d}) = \mathcal{L}_2(\mathbf{m}_t)P_1(\mathbf{m}_t|\mathbf{d}). \quad (4)$$

180 If $P_1(\mathbf{m}_t|\mathbf{d}) < P_1(\mathbf{m}_{t-1}|\mathbf{d})$, the algorithm randomly decides to evaluate $P_2(\mathbf{m}_t|\mathbf{d})$ or
 181 to reject the proposed moved with a probability $P = P_1(\mathbf{m}_t|\mathbf{d})/P_1(\mathbf{m}_{t-1}|\mathbf{d})$ of going
 182 to the second step. At the second step, the acceptance of the proposed move is computed
 183 as in the standard Metropolis-Hastings algorithm. In this work, $P_1(\mathbf{m}_t|\mathbf{d})$ and $P_2(\mathbf{m}_t|\mathbf{d})$
 184 correspond to the surface-wave dispersion solver and the 3D MT solver, respectively (see
 185 details in Section 3).

186 We will also make use of the Adaptive Metropolis (AM) approach of Haario et al.
 187 (2001) to ameliorate the problem of choosing an optimal proposal before the start of the
 188 MCMC simulation and to obtain a more efficient sampling strategy of the parameter space
 189 that exploits correlations in the model parameters. We leave the presentation of this method
 190 to Section 5, where the general sampling strategy is discussed in detail.

3 Forward Problems

3.1 The Magnetotelluric Forward Problem

In this section, we introduce the 3D magnetotelluric (MT) forward problem, the finite-element high-fidelity solver and the RB+MCMC approach to compute surrogate solutions. The reader is referred to Douglas Jr et al. (1999, 2000) and Zyserman & Santos (2000) for an in-depth treatment of the theory behind the formulation of the 3D MT problem and to (Part I; Manassero et al., 2020) for a detailed description of the surrogate approach.

3.1.1 High-fidelity solver for the MT forward problem in 3D

Using the secondary field formulation of Douglas Jr et al. (1999, 2000) and the absorbent boundary conditions defined by Sheen (1997), the MT forward problem in 3D is defined as follows:

Find \mathbf{E} and \mathbf{H} such that

$$\sigma \mathbf{E} - \nabla \times \mathbf{H} = -\mathbf{F} \quad \text{in } \Omega, \quad (5a)$$

$$i\omega\mu_0 \mathbf{H} + \nabla \times \mathbf{E} = 0 \quad \text{in } \Omega, \quad (5b)$$

$$(1 - i)P_\tau a \mathbf{E} + \nu \times \mathbf{H} = 0 \quad \text{on } \partial\Omega \equiv \Gamma, \quad (5c)$$

where \mathbf{E} is the electric field [V/m]; \mathbf{H} is the magnetic field [A/m]; μ_0 is the magnetic permeability of free space [Vs/Am]; σ is the electrical conductivity [S/m] of the medium $\Omega \in \mathbb{R}^3$ and $\Gamma \equiv \partial\Omega$ is the boundary of the domain Ω . a is defined as $a = (\sigma/2\omega\mu_0)^{1/2}$ and $P_\tau \boldsymbol{\varphi} = \boldsymbol{\varphi} - \nu(\nu \cdot \boldsymbol{\varphi})$ is the projection of the trace of any vector $\boldsymbol{\varphi}$ on Γ where ν is the unit outer normal to Γ .

High-fidelity numerical solutions to Eqs. 5 are sought via an optimized version of the finite element (FE) code developed by Zyserman & Santos (2000). In this optimized version, once the variational formulation of Eqs. 5 is discretized in terms of the FE shape functions, Eqs. 5 are converted into the following linear system of equations:

$$\mathbb{K}\mathbf{U} = \mathbf{F}, \quad (6)$$

where $\mathbb{K}^{N_{FE} \times N_{FE}}$ is a sparse and symmetric matrix (the so-called FE *stiffness matrix*) and N_{FE} is the number of degrees of freedom (usually very large). $\mathbf{F}^{N_{FE} \times 1}$ is the force vector and $\mathbf{U}^{N_{FE} \times 1}$ is a vector containing the unknown coefficients for the electric field in the whole domain. In MT, the numerical forward solution for a conductivity model requires the computation of two (typically orthogonal) components of the electromagnetic (EM) fields per frequency. Here, these components are referred to as \mathbf{U}^{S^i} and \mathbf{U}^{S^\perp} , for a frequency i . Once these solutions are computed, their coefficients and the FE shape functions are used to derive the electric and magnetic fields in the whole domain and at the surface of the Earth (for comparison with the observed data). It is worth noting that although the EM fields that satisfy Eqs. 5 are the actual solution to the forward problem, we will refer to the vector \mathbf{U} (either \mathbf{U}^{S^i} or \mathbf{U}^{S^\perp}) as the *high-fidelity* solution to the forward problem.

As previously mentioned, the overall cost of computing the high-fidelity solution has been the main limitation preventing probabilistic inversions of 3D MT data. In the following section, we briefly describe the RB+MCMC strategy introduced in our previous paper (Manassero et al., 2020) to obtain fast and accurate approximations of the high-fidelity solutions.

226

3.1.2 Surrogate solutions: A Reduced Basis + MCMC approach

227

228

229

230

231

232

233

234

235

The RB+MCMC approach combines three main elements i) a Reduced Basis (RB) method to obtain fast approximations of the high-fidelity solution; ii) an MCMC algorithm that drives the sampling of the parameter space and iii) an efficient parallel-in-parallel structure to solve the 3D MT forward problem (for both the surrogate and high-fidelity solvers). The first level of parallelization is defined by frequency, i.e. different processors are in charge of computing the forward solution for different frequencies. The second level of parallelization includes a group of processors linked to each frequency which compute (when needed) the costly high-fidelity solutions using the parallel solver *MUMPS* (Amestoy et al., 2001, 2006).

236

237

238

239

240

241

242

243

244

245

The general idea behind RB approaches is to seek for surrogate solutions as projections onto a space of small dimensionality, referred to as the *reduced basis*. We generate a reduced basis space $\mathcal{V}_{\mathcal{RB}}$ per frequency and field orientation, with dimension $N_{\mathcal{RB}} \ll N_{FE}$ and basis vectors \mathbf{V}_j . These *bases* are high-fidelity solutions of Eqs. 6 for specific realizations θ of the conductivity model, $\sigma(\mathbf{x}, \theta)$. In contrast to traditional RB approaches, these bases are not sampled in a pre-inversion stage, but rather during the MCMC inversion. In this way, each $\mathcal{V}_{\mathcal{RB}}$ is automatically updated (enriched) by adding new bases as needed during the evolution of the MCMC chain. This *online* enrichment approach circumvents the need of costly *offline* stages to build the reduced basis and increases the overall efficiency of the method (e.g. Manassero et al., 2020).

246

247

In the following, we summarize the main steps of the RB+MCM procedure. Note that items (i)–(iv) are implemented per frequency i and field orientation (S^i and S^i_{\perp}):

248

249

250

251

1. If there are bases available from an *offline* stage or from a preliminary probabilistic inversion, we load these bases as the initial basis matrix $\mathbb{V}_{\mathcal{RB}}$. Otherwise, we compute the high-fidelity solution of the starting model of the Markov chain and add it as a column vector in the initial $\mathbb{V}_{\mathcal{RB}}$.
2. For a new sample $\mathbf{m}_t = \sigma(\mathbf{x}, \theta)$, we first seek for a surrogate solution to the forward problem by solving

$$\mathbb{K}_{\mathcal{RB}}(\theta)\mathbf{a} = \mathbf{F}_{\mathcal{RB}}(\theta) \quad (7)$$

252

253

for the coefficients $\mathbf{a}(\theta)$; where $\mathbb{K}_{\mathcal{RB}}(\theta)^{N_{\mathcal{RB}} \times N_{\mathcal{RB}}} = \mathbb{V}_{\mathcal{RB}}^T \mathbb{K}(\theta) \mathbb{V}_{\mathcal{RB}}$ is the RB matrix, $\mathbf{F}_{\mathcal{RB}}(\theta)^{N_{\mathcal{RB}} \times 1} = \mathbb{V}_{\mathcal{RB}}^T \mathbf{F}(\theta)$ is the RB force vector and $\mathbb{V}_{\mathcal{RB}}^{N_{FE} \times N_{\mathcal{RB}}} = [\mathbf{V}_1, \mathbf{V}_2, \dots, \mathbf{V}_{N_{\mathcal{RB}}}]$ is the matrix of basis vectors of $\mathcal{V}_{\mathcal{RB}}$. The surrogate solution, $\mathbf{U}_{\mathcal{RB}}(\theta)$, is then found as a linear combination of the basis vectors in $\mathcal{V}_{\mathcal{RB}}$ by substituting the coefficients $\mathbf{a}(\theta)$ into the following equation:

$$\mathbf{U}_{\mathcal{RB}}(\mathbf{x}, \theta) = \sum_{j=1}^{N_{\mathcal{RB}}} a_j(\theta) \mathbf{V}_j = \mathbb{V}_{\mathcal{RB}} \mathbf{a}(\theta). \quad (8)$$

254

255

Since the linear system of Eqs. 7 is of size $N_{\mathcal{RB}} \ll N_{FE}$, its computational cost is only a small fraction of the time consumed in solving Eqs. 6.

3. The following relative error is computed to assess the accuracy of the surrogate (Quarteroni et al., 2015; Hesthaven et al., 2016):

$$\mathbf{R}_{\mathcal{RB}} := \frac{\|\mathbb{K} \mathbf{U}_{\mathcal{RB}} - \mathbf{F}\|}{\|\mathbf{F}\|}, \quad (9)$$

256

257

258

259

260

where $\|\cdot\|$ is the L_2 norm.

4. The surrogate solution is considered admissible if the $\mathbf{R}_{\mathcal{RB}}$ verifies $\mathbf{R}_{\mathcal{RB}} \leq \beta$ for a prescribed tolerance β .
5. If all the errors $\mathbf{R}_{\mathcal{RB}}$ are smaller than β , we accept $\mathbf{U}_{\mathcal{RB}}^{S^i}$ and $\mathbf{U}_{\mathcal{RB}}^{S^i_{\perp}}$ as good approximations of the high-fidelity solution for all frequencies. In this case, the

261 corresponding approximate likelihood, $\bar{\mathcal{L}}_2(\mathbf{m}_t)$, is computed and the sample is ei-
 262 ther accepted or rejected according to the Metropolis-Hastings (MH) criterion.
 263 6. In the case of any $\mathbf{R}_{RB} \gg \beta$, the high-fidelity FE solution for that frequency and
 264 component of the EM field is computed for \mathbf{m}_t and added as a new basis vector
 265 to enrich the corresponding space \mathcal{V}_{RB} . Since the posterior probabilities of the pro-
 266 posed sample \mathbf{m}_t and that of the current sample \mathbf{m}_{t-1} are no longer comparable
 267 (i.e. they were computed with different solvers, FE and RB, respectively), we re-
 268 compute the surrogate solution (and the associated likelihood) at sample \mathbf{m}_{t-1}
 269 using the newly enriched RB space. If \mathbf{m}_t is rejected by the MH criterion, a new
 270 trial \mathbf{m}_t^* is proposed in the vicinity of \mathbf{m}_t and its likelihood is computed with the
 271 newly enriched RB space. This new trial \mathbf{m}_t^* is accepted/rejected according to a
 272 modified Metropolis ratio to account for the delayed rejection (i.e. two propos-
 273 als) step (see e.g. Haario et al., 2006; Mira et al., 2001).

274 As explained in Manassero et al. (2020), the last step above is required to preserve
 275 the ergodicity of the algorithm, but it is not the only possible option. We refer the reader
 276 to our previous work (Manassero et al., 2020) for further details on the combined RB+MCMC
 277 approach and additional functionalities to improve the efficiency of the method (e.g. use
 278 of variable tolerances and Singular Value Decomposition of the basis).

279 3.2 The Surface-Wave Forward Problem

280 Surface waves provide one of most valuable data sets to study the lithospheric struc-
 281 ture (e.g. Yang et al., 2008; Huang et al., 2009; J. Afonso et al., 2013a). One of the most
 282 common approaches involves the generation of dispersion curves or maps and the sub-
 283 sequent inversion of these curves for the velocity structure at depth. Here we compute
 284 dispersion curves as functions of 1D vertical velocity structures with a modified version
 285 of the forward code *disp96* (Herrmann & Ammon, 2002; J. C. Afonso et al., 2013b; J. C. Afonso,
 286 Rawlinson, et al., 2016). We compute anelastic wave velocities (V_s and V_p) of mantle
 287 rocks as (J. C. Afonso et al., 2005, 2008, 2010):

$$V_s = V_{s0}(T, P)[1 - (1/2)\cot(\alpha\pi/2)Q_s^{-1}(T_o, T, P, d)], \quad (10)$$

$$V_p = V_{p0}(T, P)[1 - (2/9)\cot(\alpha\pi/2)Q_s^{-1}(T_o, T, P, d)], \quad (11)$$

288 where V_{s0} and V_{p0} are the unrelaxed, high-frequency (anharmonic) wave velocities at a
 289 given temperature (T) and pressure (P) (cf. J. C. Afonso et al., 2010). Without loss of
 290 generality, here we compute them as

$$V_{p0} = V_p^{ref} + \frac{\partial V_p}{\partial T} \Delta T + \frac{\partial V_p}{\partial P} \Delta P, \quad (12)$$

$$V_{s0} = V_s^{ref} + \frac{\partial V_s}{\partial T} \Delta T + \frac{\partial V_s}{\partial P} \Delta P, \quad (13)$$

where V_p^{ref} and V_s^{ref} are reference velocities at T_{ref} and P_{ref} ; $\Delta T = T - T_{ref}$ and
 $\Delta P = P - P_{ref}$. The factor Q_s^{-1} is obtained as (Jackson et al., 2002; Jackson & Faul,
 2010)

$$Q_s^{-1} = A \left[\frac{T_o}{d} \exp\left(\frac{-E + VP}{RT}\right) \right]^\alpha, \quad (14)$$

291 where T_o is the oscillation period, d is grain size, E is the activation energy, V is the ac-
 292 tivation volume, α is an empirical exponent, A is a pre-exponential constant and R is
 293 the universal gas constant. Although more sophisticated/realistic approaches for com-
 294 puting anelastic seismic velocities are possible (e.g. Matas & Bukowinski, 2007; Khan
 295 et al., 2008; J. Afonso et al., 2013a; J. C. Afonso et al., 2013b; Vozar et al., 2014), the
 296 set represented by Eqs. 10-14 is sufficient for the goals of this paper.

4 Model Parameterization and Discretization

A key difficulty in the joint inversion of two or more disparate geophysical data sets is how to define the interdependence between model parameters in an internally consistent manner. For instance, if our goal was to jointly invert first arrivals of compressional waves (V_p) and gravity anomalies (a common approach in geophysics), we would need to answer the following question: how is V_p related to bulk density in our medium? A typical assumption in this case is considering a linear correlation between V_p and density (e.g. Birch, 1961, 1964; Feng et al., 1986; Yasar & Erdogan, 2004). While this is a popular and practical assumption, the actual relationship between V_p and density also depends on temperature, pressure and bulk composition (see e.g. J. Afonso et al., 2013a; Guerri et al., 2016). Several authors therefore distinguish between primary and secondary parameters (e.g. Bosch, 1999; Khan et al., 2006; J. Afonso et al., 2013a). The latter are the most commonly used in geophysical inversions and refer to those that enter the governing equations of the forward problems (e.g. V_p , density, electrical conductivity); the former are more fundamental in their nature and thus control the values of the secondary ones (e.g. temperature, porosity, pressure).

In the case of joint inversions of SW and MT data, the primary parameters controlling both the seismic velocities and electrical conductivity (σ) in the mantle are temperature (T), bulk major-element composition (C) and pressure P (e.g. Jones et al., 2009; Fullea et al., 2011; R. Evans, 2012; Selway, 2014). Using empirically calibrated equations of state of the type $V_p(T, P, C)$, $V_s(T, P, C)$ and $\sigma(T, P, C)$, and thermodynamic constraints, we can establish direct relationships between the primary and secondary parameters (Bosch, 1999; Xu et al., 2000; Khan et al., 2006; Jones et al., 2009; Yoshino, 2010; Fullea et al., 2011). Since the electrical conductivity is also highly sensitive to hydrogen content, minor conductive constituents and localized melt/fluid pathways, we can explicitly write $\sigma(T, P, C, X)$, where X stands for any factor other than the bulk major-element composition of the rock. This distinction emphasizes the fact that although both seismic velocities and electrical conductivity can constrain the background T - P - C field, the electrical conductivity offers sensitivity to additional factors. The chosen model parameterization should thus be able to accommodate representative variations in both primary parameters (that simultaneously control V_p , V_s and σ) and those responsible for conductivity anomalies above the background values. At the same time, as in any other inverse geophysical problem, the choice of model parameterization needs to be based on the principles of i) flexibility, ii) parsimony, iii) parameter identifiability and iv) suitability for the intended use.

With all of these in mind, and given our particular interest in lithospheric-scale imaging, we focus on a mixed parameterization of the conductivity distribution as the superposition of two contributions: a *background* conductivity related to the long-wavelength thermo-physical state of the lithosphere and an *anomalous* conductivity distribution associated with the presence of features such as fluid pathways, melt-rich regions, hydrogen-rich domains, anomalous mineral assemblages, etc. Following J. Afonso et al. (2013a); J. C. Afonso et al. (2013b), we choose the depth to the lithosphere-asthenosphere boundary (LAB) and the bulk mantle composition as the main model parameters to constraint the background velocity and conductivity structures. We discuss this parameterization in more detail in Section 4.1. In order to account for smaller-scale conductivity anomalies superimposed on the background, we use a more standard parameterization based on conductivity nodes. This parameterization is only relevant to the MT forward problem and it is described in detail in Section 4.2. As shown in the numerical examples of Section 6, the advantage of using this combined parameterization is that a rapid convergence is achieved by using the LAB depths to constrain the first-order conductivity background at the beginning of the inversion. Once this first-order convergence has been achieved, the nodal values are used to locally modify the background to fit the smaller-scale features of the data.

Table 1: Parameters used in the computation of V_{s0} and V_{p0} .

T_{ref}	800.0°C
P_{ref}	0 Gpa
$\partial V_p/\partial T$	-5.1×10^{-4} (km/sC)
$\partial V_p/\partial P$	0.110 (km/sGPa)
$\partial V_s/\partial T$	-3.3×10^{-4} (km/sC)
$\partial V_s/\partial P$	0.03 (km/sGPa)

350

4.1 Background parameterization

The 3D numerical model is made up of a collection of M_{col} columns (see Fig 1.b). Each individual column is characterized by its own LAB depth. Here, we identify the LAB with the depth to the 1250°C isotherm (cf. J. C. Afonso, Moorkamp, & Fullea, 2016). In order to obtain the background conductivity structure from the LAB structure, we first compute the thermal profile of each column by solving the steady-state heat transfer problem with Dirichlet boundary conditions at the surface ($T_0=10^\circ C$) and bottom of the lithosphere ($T_{LAB}=1250^\circ C$). For simplicity, but without loss of generality, we assume a linear temperature gradient between the LAB and 410 km depth, where the temperature is fixed at $T_{410}=1550^\circ C$. This gradient is extrapolated to the bottom of the numerical domain (460 km). A pressure profile is also computed in each column using the following quadratic lithostatic-type approximation:

$$P(z) = 0.99 \times (4.4773 \times 10^{-3} z^2 + 3.2206 \times 10^4 z - 1.284278 \times 10^8), \quad (15)$$

351

where P is pressure in Pa and z is depth in meters.

352

353

354

355

356

357

358

359

360

361

362

363

As a further simplification, we assume a dry and homogeneous mantle composition with the following mineral modes: 56, 18.2, 10.8 and 15 vol% for olivine, orthopyroxene, clinopyroxene and garnet, respectively. While more realistic/sophisticated approaches to map major-element composition into mineral phases should be used when working with real data (e.g. Khan et al., 2006; J. Afonso et al., 2013a; J. C. Afonso et al., 2013b; J. C. Afonso, Rawlinson, et al., 2016; Jones et al., 2017), this simplification does not affect the main results and conclusions of this paper. The electrical conductivity for each mineral phase is obtained using Eq. A3 with parameters specified in Table A1 and the bulk electrical conductivity (i.e. that of the mineral aggregate or rock) of each FE cell in the mantle is computed using the Hashin–Shtrikman averaging scheme (Hashin & Shtrikman, 1962, 1963). In the numerical examples shown here, the resistivity in the crust (Moho at 49 km depth) is held constant and equal to 20,000 Ωm .

For the surface-wave dispersion problem, each 1D column is further subdivided into 60 layers, each with constant density and wave velocities. The density of each layer is computed as a function of T and P values at the depth of its mid-point as follows:

$$\varrho(P, T) = \varrho_0 + 1 - \alpha(T - T_0) + \beta(P - P_0), \quad (16)$$

364

365

366

367

368

369

370

with $\varrho_0 = 3355 \text{ kg/m}^3$, $T_0 = 10^\circ C$, $P_0 = 0 \text{ Pa}$, $\alpha = 3.6 \times 10^{-5} \text{ 1/}^\circ C$ and $\beta = 1.1 \times 10^{-11} \text{ 1/Pa}$. For a particular layer, the V_p and V_s are obtained using Eqs. 10 and Eq. 14 with the following values: $A_v = 750 \text{ s}^{-\alpha} \mu \text{ m}^\alpha$, $\alpha = 0.26$, $E = 424 \text{ kJmol}^{-1}$, $V = 1.3 \times 10^{-5} \text{ m}^3 \text{ mol}^{-1}$ and grain size $d = 5.0 \mu \text{ m}$. Given the periods of interest for surface waves, we adopt $T_o = 50 \text{ s}$ in Eq. 14 (Liu et al., 1976; Lebedev & Van Der Hilst, 2008; Moorkamp et al., 2020). The values for the parameters used in Eqs. 12 and 13 are listed in Table 1 (after J. C. Afonso et al., 2010).

371

4.2 Node-based parameterization

372

373

374

375

376

377

378

379

380

381

382

383

384

Any conductivity anomaly that departs from the background is described with N_{nodes} nodes located within the numerical domain. In order to define the nodal locations (Fig. 8), the domain is first sub-divided into horizontal layers of variable thickness. The mid-points of these layers correspond to the nodal depths. Considering that bodies with dimensions smaller than the electromagnetic skin depth cannot be resolved by the MT data, the horizontal distance between different locations within each layer is chosen relative to the skin depth for the range of periods and apparent resistivities shown in the observed data (see for example Figs. 13). The parameters of interest to be retrieved by the inversion are the conductivity values of these nodes. During the probabilistic inversion, the nodal values are interpolated to each FE cell of the numerical domain via kriging interpolation (see e.g. Cressie, 1993; Omre, 1987; Williams & Rasmussen, 1996) using spatially varying correlation lengths (Section B1). Details about the implementation of the interpolation are given in Section Appendix B of the Appendix.

385

386

387

388

389

390

391

392

393

394

395

396

Intuitively, the range of anomalous conductivity values for the nodes should allow for positive and negative perturbations with respect to the background. However, as the electrical conductivity values can span several orders of magnitude, nodal values are typically obtained from proposal distributions defined in logarithmic scale (e.g. Jeffreys and log-normal distributions). Since the domain of the logarithmic function is the set of all positive real values, the sampled anomalous conductivity values (in linear scale) are always positive. In practice, this is not a limitation, as resistive structures (i.e. negative deviations from the background) are generally determined solely by changes in the thermo-physical state (e.g. temperature and/or composition changes) whereas anomalous features of interest, such as presence of melt and/or fluid, hydrogen content, grain-boundary graphite films and interconnected sulfides produce positive conductivity anomalies (e.g. Selway, 2014; Hu et al., 2017).

397

5 Sampling Strategy

398

399

400

401

402

403

404

405

406

407

408

409

The sampling strategy is specifically tailored to take advantage of the differential sensitivities of the SW and MT data sets to the conductivity structure of the lithosphere. With this in mind, we subdivide the MCMC inversion into four main stages. The first stage aims to constrain the background conductivity associated with the first-order temperature structure defined by the LAB depths (if we were interested in inverting for bulk chemical composition, we would also sample this parameter). In the second stage, conductivity anomalies over the background start to be sampled. During these first two stages, we sample both the LAB depths and the conductivity nodes using a *metropolized-independent* sampler. Once enough information (i.e. enough samples) has been acquired for both sets of parameters, we incorporate adaptive strategies to efficiently sample the full parameter space during the third and fourth stages. We briefly describe each of these stages below.

410

5.1 First stage: focus on background fields

411

412

413

414

415

416

417

418

419

- i Randomly select a column in the 3D domain using a *metropolized-independent sampler*.
- ii Randomly propose an LAB depth for that column from its proposal distribution.
- iii Re-compute the temperature and pressure profiles and update the conductivity and wave velocities (\mathbf{m}_t), as explained in Section 4.1.
- iv Evaluate the first partial likelihood $P_1(\mathbf{m}_t|\mathbf{d})$ with the SW solver.
- v Evaluate $P_2(\mathbf{m}_t|\mathbf{d})$ with probability $P = P_1(\mathbf{m}_t|\mathbf{d})/P_1(\mathbf{m}_{t-1}|\mathbf{d})$ using the MT forward solution:
 - (a) Seek for a surrogate RB solution to the 3D MT forward problem (Section 3.1.2).

- 420 (b) If $\mathbf{R}_{\text{RB}} < \beta$ for all frequencies, \mathbf{m}_t is accepted or rejected according to the Metropolis-
 421 Hastings criterion.
- 422 (c) If any $\mathbf{R}_{\text{RB}} > \beta$, the high-fidelity FE solution is computed at \mathbf{m}_t . The RB sur-
 423 surrogate is recomputed at \mathbf{m}_{t-1} and the algorithm proposes a new move in the vicin-
 424 ity of \mathbf{m}_t whose acceptance is evaluated with a Delayed Rejection criterion (Sec-
 425 tion 3.1.2).

426 5.2 Second stage: conductivity nodes begin to be sampled

427 When the number of MCMC steps reaches a predefined number of simulations (*LAB-*
 428 *stage*):

- 429 i Randomly chose a type of parameter to sample (i.e. LAB depths or nodes) at each
 430 MCMC step.
- 431 ii If chosen parameter = LAB, the algorithm follows the **first stage**.
- 432 iii If chosen parameter = conductivity nodes:
- 433 (a) Randomly select n_1 nodes at a time, with all nodes having the same probability
 434 of being chosen.
- 435 (b) Assign a random conductivity value to each node from their individual proposal
 436 distributions.
- 437 (c) Update the 3D conductivity model via kriging interpolation.
- 438 (d) $P_1(\mathbf{m}_t|\mathbf{d})$ remains unchanged, i.e. it only changes when a new LAB value is pro-
 439 posed.
- 440 (e) Evaluate $P_2(\mathbf{m}_t|\mathbf{d})$ with the MT solver following items (a)-(c) of the **first stage**.

441 5.3 Third stage: adaptive strategy for the LAB depths

442 When the number of MCMC steps reaches a predefined number of simulations (*LAB-*
 443 *adapt*):

- 444 i Compute a new multivariate Gaussian proposal distribution (via the Adaptive Metropo-
 445 lis algorithm of Haario et al. (2001)) using the history of the MCMC chains. This
 446 proposal now has information about spatial correlations in the LAB.
- 447 ii Randomly chose a type of parameter to sample (i.e. LAB depths or nodes) at each
 448 MCMC step.
- 449 iii If chosen parameter = LAB:
- 450 (a) Randomly select m columns at a time, with all columns having the same prob-
 451 ability of being chosen.
- 452 (b) Propose a new sample for the selected LAB depths using the global multivariate
 453 Gaussian proposal.
- 454 (c) Follow items (iii)-(v) of the **first stage**.
- 455 iv If chosen parameter = conductivity nodes, the algorithm follows items (a)-(f) of the
 456 **second stage**.

457 5.4 Fourth stage: adaptive strategy for the conductivity nodes

458 When the number of MCMC steps reaches a predefined number of simulations (*nodes-*
 459 *adapt*):

- 460 i Compute a multivariate log-normal proposal distribution via the Adaptive Metropo-
 461 lis algorithm using the MCMC chains of all nodes.

- 462 ii Randomly chose a type of parameter to sample (i.e. LAB depths or nodes) at each
 463 MCMC step.
- 464 iii If chosen parameter = LAB, follow item (iii) of the **third stage**.
- 465 iv If chosen parameter = conductivity nodes:
- 466 (a) Randomly select n_2 nodes with a *metropolized-independent sampler*.
- 467 (b) Use the multivariate log-normal distribution to propose new conductivity values
 468 for the n_2 random nodes with probability $q(\cdot)$ defined in Eq. C2.
- 469 (c) Follow items (c)-(f) of the **second stage**.

470 The first stage only needs a moderate number of models to significantly reduce the
 471 original range of possible LAB values. This rapid convergence is due to the strong com-
 472 bined sensitivity of SW and MT to the background field; it also allows the MCMC in-
 473 version to focus on the last three stages (i.e. on conductivity anomalies not related to
 474 the background *T-P-C* conditions) while still allowing a continuous improvement of the
 475 background field. Additional gain in convergence efficiency is obtained with adaptive sam-
 476 pling strategies applied to both LAB and conductivity nodes. The implementation of
 477 these strategies is almost imperative given the high-dimensionality of the problem. While
 478 more advanced sampling strategies (e.g, parallel tempering, differential evolution, auto-
 479 regressive chains) can be implemented to further improve efficiency, we deliberately use
 480 this practical (and basic) four-step adaptive strategy to test our joint inversion algorithm
 481 under adverse circumstances.

482 6 Numerical Examples

483 In this section we consider two numerical examples of joint probabilistic inversion
 484 of SW and 3D MT data within the context of whole-lithosphere structure. The synthetic
 485 data correspond to two complex large-scale lithospheric models with dimensions $1600 \times$
 486 1600×460 km (Figs. 1 and 8). In both cases, the computational domain is discretized
 487 with $40 \times 40 \times 20$ finite elements.

488 6.1 Synthetic Data

489 The MT synthetic data are the off-diagonal apparent resistivities and phases for
 490 Example 1 and the full impedance tensor for Example 2. Each dataset is computed for
 491 12 periods between 3.2 and 10^4 seconds at 400 stations. The stations are located on a
 492 grid of 20×20 (Fig. 1.a) with an inter-station distance of 80 km. The data errors are
 493 assumed to be uncorrelated and normally distributed. In Example 1 we use a standard
 494 deviation of 12% for the apparent resistivities and 1.5 degrees for the phases, whereas
 495 in Example 2 the standard deviation is assumed as 5% of $\max(|Z_{xx}|, |Z_{xy}|)$ for the com-
 496 ponents Z_{xx} and Z_{xy} of the impedance tensor, and 5% of $\max(|Z_{yy}|, |Z_{yx}|)$ for the com-
 497 ponents Z_{yy} and Z_{yx} .

498 For the case of the SW, the synthetic data are the normal mode Rayleigh wave phase
 499 velocities for periods between 15 and 175 seconds, computed at the locations of the MT
 500 stations. We assume normally distributed data errors with a representative standard de-
 501 viation (std) of 20% of the period for Example 1 (that is, $2 * std = 10m/s$ for 25s and
 502 $2 * std = 80m/s$ for 200s). For the second example, we consider a standard deviation
 503 of 1% of the velocity in meters, which is comparable to the data errors expected for real
 504 SW data in dense arrays (Moorkamp et al., 2010; Yang & Forsyth, 2006; Wang et al.,
 505 2020).

506 To minimise the so-called ‘inversion crime’ (Kaipio & Somersalo, 2006), we com-
 507 pute the actual synthetic data of the first example with a finer FE mesh than that used
 508 in the inversion. In the second example, while the models used during the inversion are

509 obtained via interpolation of the nodes' values, the MT data is generated with the true
 510 conductivity value for each FE cell. While this avoids the inversion crime, it also implies
 511 that a perfect data fit may not be achievable.

512 6.2 Data Misfits

513 The SW and MT misfits, ϕ_{SW} and ϕ_{MT} , are computed as

$$\phi_{SW} = -\frac{1}{2} \sum_{i=1}^{N_{sta}} \sum_{j=1}^{N_{per}} \left(\frac{g_{ij} - d_{ij}}{std_{ij}} \right)^2 \quad (17a)$$

$$\phi_{MT} = -\frac{1}{2 \cdot N_{dat}} \sum_{i=1}^{N_{sta}} \sum_{j=1}^{N_{per}} \left(\frac{g_{ij} - d_{ij}}{std_{ij}} \right)^2 \quad (17b)$$

514 where N_{sta} and N_{per} are the number of stations and periods for each dataset; d_{ij} and
 515 g_{ij} correspond to the observed and computed data (with the MT or the SW forward)
 516 for station i and period j , and std_{ij} is the standard deviation for data d_{ij} . N_{dat} is the
 517 total number of MT data used for each station and frequency, e.g. $N_{dat} = 8$ when we
 518 invert for the real and imaginary parts of the full impedance tensor. The factor $1/N_{dat}$
 519 is used here to assure that both data sets have similar absolute contributions in the joint
 520 inversion, i.e. that their weights in the overall misfit are not controlled by the number
 521 of data points in one of the data sets (e.g. Kalscheuer et al., 2013).

522 6.3 Example 1: Large-scale Thermal Lithospheric Structure

523 6.3.1 Model Setup

524 The inversion area is sub-divided into 18×18 columns (white squares in Fig. 1.b)
 525 of size $80 \times 80 \times 460$ km. Each column is comprised of $4 \times 4 \times 20$ FE cells. The model
 526 parameters are the depths to the LAB of the 324 columns within the inversion area, i.e.
 527 there is one model parameter per column. The true conductivity model is shown in Figs.
 528 1 and is controlled by the subsurface thermal structure. The goal of this example is to
 529 assess the identifiability of the background conductivity distribution (via the recovery
 530 of the model parameters) from noisy MT and SW data. Accordingly, we only use the
 531 LAB parameterization in the first and third stages (Sections 5.1 and 5.3).

532 6.3.2 Prior and proposal distributions

533 The priors for the LAB depths are uniform distributions defined in a range of ± 70
 534 km, centered on the true value of each column. The proposals used in the first stage of
 535 the inversion are Gaussian distributions centered on the current sample with a standard
 536 deviation of 20 km. The proposal is adapted in the third stage and therefore it becomes
 537 a multivariate Gaussian distribution that reflects the spatial correlations between LAB
 538 values of all columns (see Section 5.3). The initial model (i.e. starting point of the MCMC
 539 inversion) has a flat LAB located at 180 km depth.

540 6.3.3 Inversion results

541 We ran a total of 600,000 MCMC simulations using 2 processors (Intel(R) Xeon(R)
 542 CPU E5-2680 v3 @ 2.50GHz processors) per frequency and variable RB tolerances of $\beta =$
 543 0.07 for the first 50,000 MCMC steps and $\beta = 0.05$ for the rest of the simulation. De-
 544 spite the small number of processors used, the joint inversion took only 25 hs, with a stag-
 545 gering average of 0.15 seconds per simulation. This means $> 99.5\%$ gain in computa-
 546 tional efficiency compared to the high-fidelity solution (~ 30 secs). For the same model,
 547 and using the same number and type of processors, the RB+MCMC inversion of MT
 548 data only (see Manassero et al., 2020) took ~ 30 days (an average of 1.03 seconds per

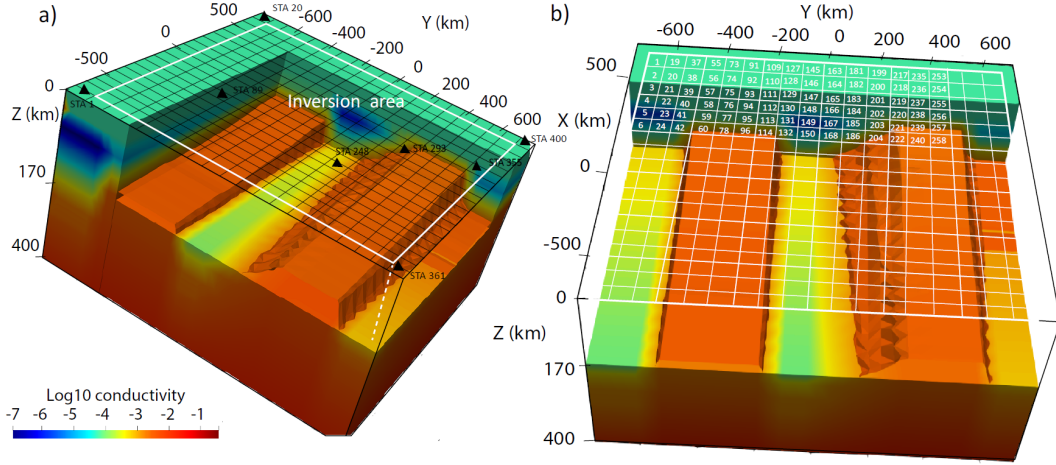


Figure 1. 3D rendering views of the true conductivity structure where the iso-surface of $-2.8 \log_{10} \text{ S/m}$ is plotted as a reference. The white rectangle in (a) indicates the region used for the inversion. Panel (a) illustrates the 20×20 station-grid in black and eight of the 400 stations (black triangles). The model parameters are the depths to the LAB of 324 columns. Panel (b) displays the location of these columns (white small squares) and 96 column-parameters as a reference. The reader is referred to Section 4.1 for details on the parameterization.

549 MCMC iteration) and convergence was achieved after 2,500,000 MCMC simulations. This
 550 dramatic gain in efficiency of the joint inversion is due mainly to i) the implementation
 551 of the CM algorithm, ii) the use of adaptive MCMC strategies and iii) the high sensi-
 552 tivity of SW data to the background thermal structure.

553 The posterior PDFs of 60 of the 324 parameters are shown in Figure 2. The data
 554 PDFs for the dispersion curves at two illustrative stations and the data PDFs for MT
 555 at one station are shown in Figs. 3 and Figs. 4, respectively. Additional results can be
 556 found in the Supplementary material. The results clearly show that the posterior PDFs
 557 for all parameters are well behaved (i.e. single valued and approximately Gaussian) and
 558 include the true solution, which is always close to the peaks of the PDFs. The result-
 559 ing uncertainties affecting the LAB values are comparable to those obtained in real in-
 560 versions (e.g. J. C. Afonso, Moorkamp, & Fullea, 2016; A. Zhang et al., 2019). The data
 561 fit is excellent for both data sets (see Figs. 3 and 4).

562 The *maximum a posteriori* (MAP) and mean models are shown in Figs. 5, together
 563 with the 95% confidence intervals of the posterior PDFs. The root-mean-square (rms)
 564 values of the *maximum a posteriori* and mean conductivity models, as well as the rms
 565 for the LAB structure, are included in Table 2. As a comparison, we have also included
 566 the rms values obtained for the same model after the RB+MCMC inversion of 3D MT
 567 data only (see Manassero et al., 2020), which are considerable higher than those obtained
 568 with the joint inversion.

569 The evolution of the misfits for MT and SW data is shown in Fig. 6. The number
 570 of bases computed per frequency and field orientations are shown in Fig. 7. In all
 571 cases, a rapid increment in the basis size is observed during the first 100,000 simulations,
 572 which correlates with a rapid decrease in the overall misfits (Fig. 6). This rapid incre-
 573 ment in the number of basis is the combination of two factors: i) the starting point of
 574 the inversion is far from the high probability region and ii) the initial proposal distri-
 575 bution is not optimal and of large variance. The MCMC algorithm thus samples a wide
 576 spectrum of models in its attempt to locate the best paths to the high probability re-

Table 2: Root-mean-square (rms) values of the mean and MAP conductivity and LAB models with respect to the true model. The rms values obtained after the RB+MCMC inversion of 3D MT data only are also included (extracted from Manassero et al., 2020).

	RMS conductivity ($\log_{10} \Omega m$)		RMS LAB depth (km)	
	Best Model	Mean Model	Best Model	Mean Model
Joint RB+MCMC	0.08	0.02	6.89	2.21
RB+MCMC	0.19	0.15	21.20	17.01

577 gions. During this exhaustive exploration, the moves or ‘jumps’ through the parameter
 578 space are large. Consequently, the resulting conductivity models are significantly differ-
 579 ent from each other and the surrogate needs to be constantly enriched in order to pro-
 580 duce accurate solutions for all possible models.

581 After $\sim 150,000$ MCMC steps, the basis size reaches a *plateau* (i.e. saturation of
 582 the surrogate) for all frequencies and orientations. This means that i) the chain has reached
 583 the high probability regions and ii) the RB surrogate is “rich enough” to be able to del-
 584 iver accurate solutions within these regions (as only a small number of new bases are
 585 subsequently required). At this point, we could stop the adaptation or enrichment of the
 586 surrogate without compromising the accuracy of the final solution.

587 These results demonstrate that our RB+MCMC approach successfully solves the
 588 joint probabilistic inversion problem and retrieves the first order conductivity structure
 589 (and associated uncertainties) from noisy MT and SW data. Moreover, we demonstrate
 590 that the addition of the SW data increases the overall efficiency of the algorithm and sig-
 591 nificantly reduces the range of acceptable conductivity models compared to those obtained
 592 from the inversion of MT data only.

593 6.4 Example 2: Large-scale Lithospheric Structure with Conductivity 594 Anomalies

595 6.4.1 Model setup

596 The true conductivity model (Fig. 8) includes the lithospheric model of Section 6.3
 597 as a background (with an additional cut-off for resistivity values higher than $20,000 \Omega m$)
 598 plus three additional and localized conductive anomalies. There are 1155 conductivity
 599 nodes (black dots in Fig. 8.a) sparsely located within the inversion volume ($1440 \times 1440 \times$
 600 410 km), which is discretized into 324 columns. The vector of model parameters there-
 601 fore contains 324 LAB values and 1155 nodal conductivity values. The conductivity value
 602 of each numerical cell is obtained by adding the background conductivity derived from
 603 the LAB structure (Section 4.1) and the anomalous conductivity obtained after inter-
 604 polation of the nodal values (Section 4.2). The goal here is to assess the identifiability
 605 of the true conductivity structure, including background and conductivity anomalies, from
 606 noisy 3D MT and SW measurements.

607 6.4.2 Prior and proposal distributions

608 The prior and proposal distributions for the LAB parameters are the ones defined
 609 in Section 6.3.2. For the conductivity nodes, we use Gaussian prior distributions cen-
 610 tered on the background conductivity value (in log-scale) with a standard deviation of
 611 $1.5 \log_{10}(S/m)$. This prior information behaves as a regularization term, i.e. it penal-
 612 izes the introduction of anomalies that are not required by the data. The initial proposal
 613 distributions are log-normal (Eq. C1) centered on the current node value m_{t-1}^i with stan-

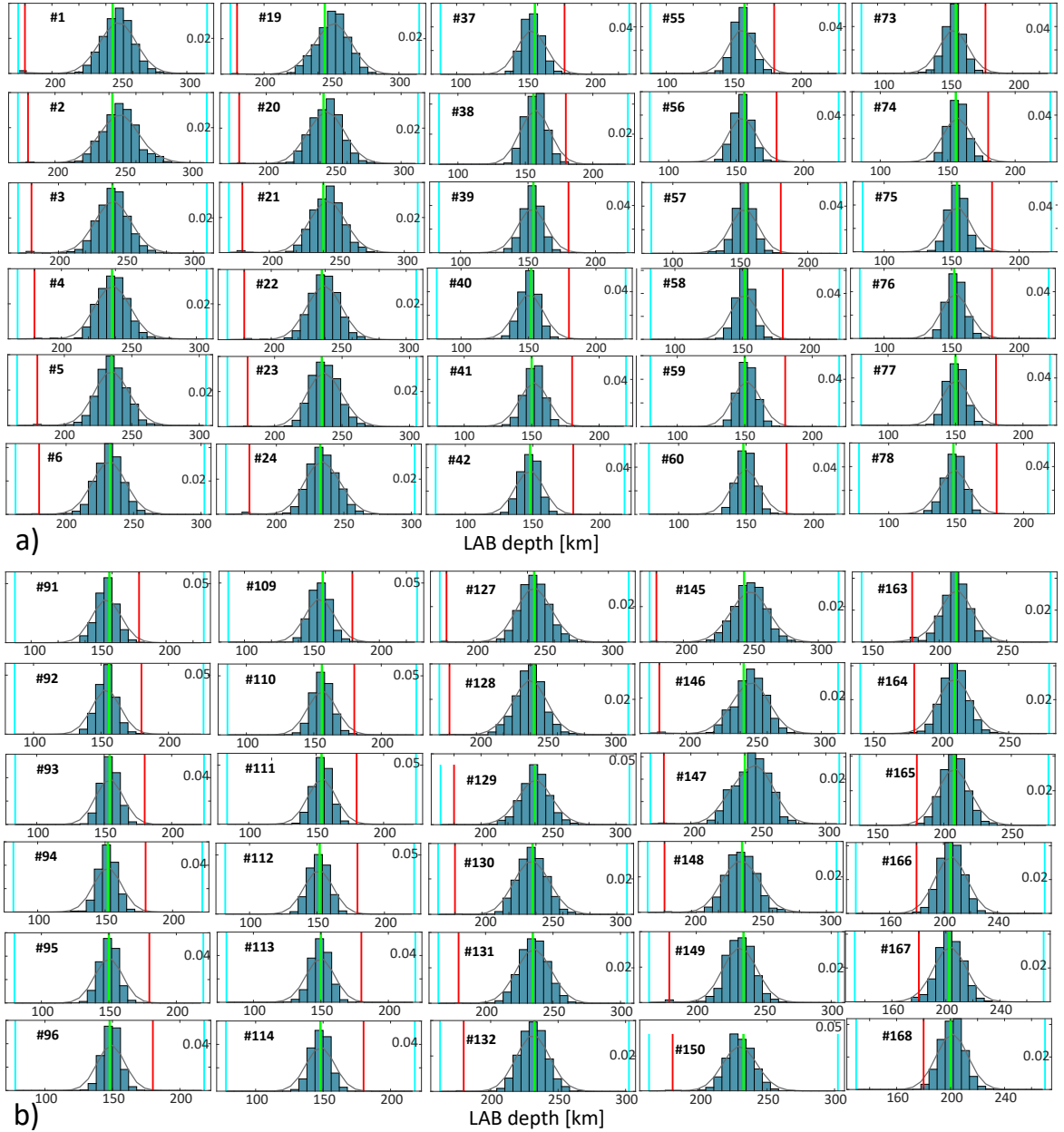


Figure 2. Marginal posterior PDFs (blue bars) of 60 model parameters obtained after 600,000 RB+MCMC simulations. The real value, starting value and prior bounds of each parameter are shown in green, red, and light blue vertical lines, respectively. The best Gaussian fits to the real PDFs given by the histograms are shown in black lines. The numbers within each panel correspond to the columns highlighted in Fig. 1.b.

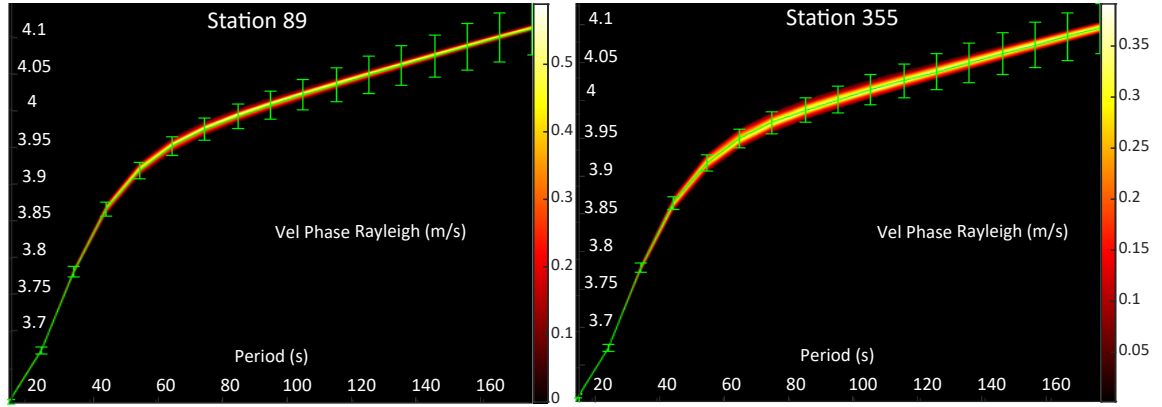


Figure 3. Posterior PDFs of Rayleigh dispersion curves for stations (a) 89 and (b) 355. Synthetic data and error bars are plotted in green. The location of the stations are shown in Fig. 1.a.

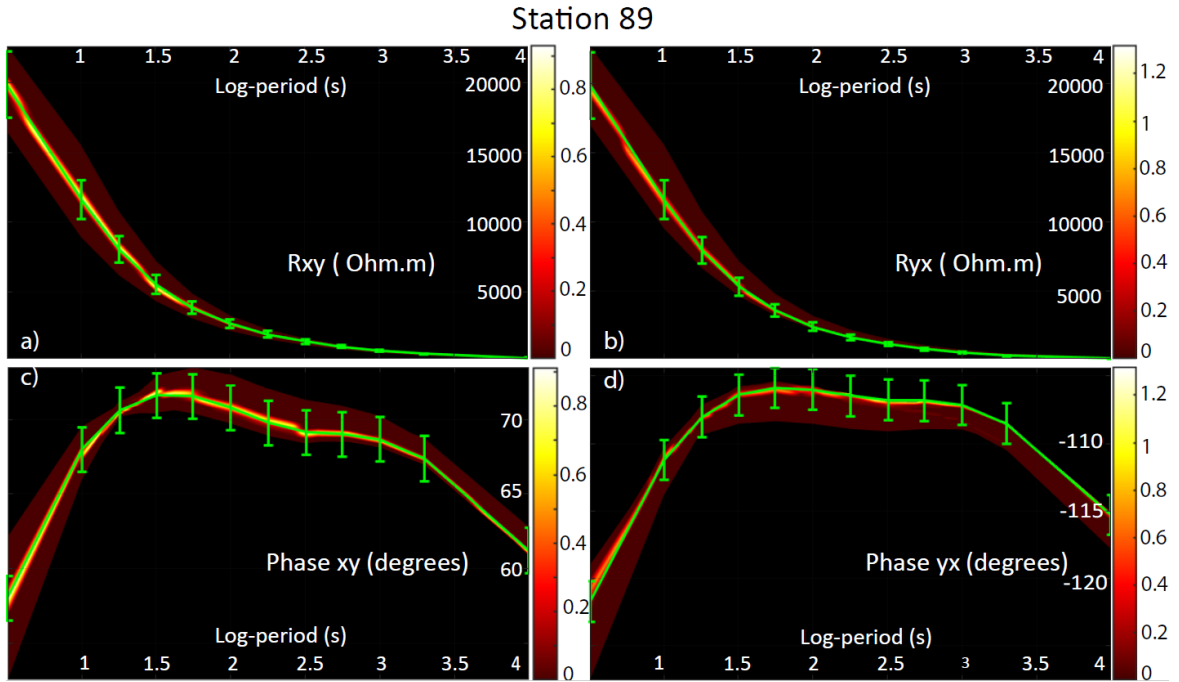


Figure 4. Posterior PDFs of MT data for station 89. Synthetic data and error bars are plotted in green. (a)-(b) Posterior PDFs of the off-diagonal apparent resistivities. (c)-(d) Posterior PDFs of the off-diagonal apparent phases. The location of the stations are shown in Fig. 1.a.

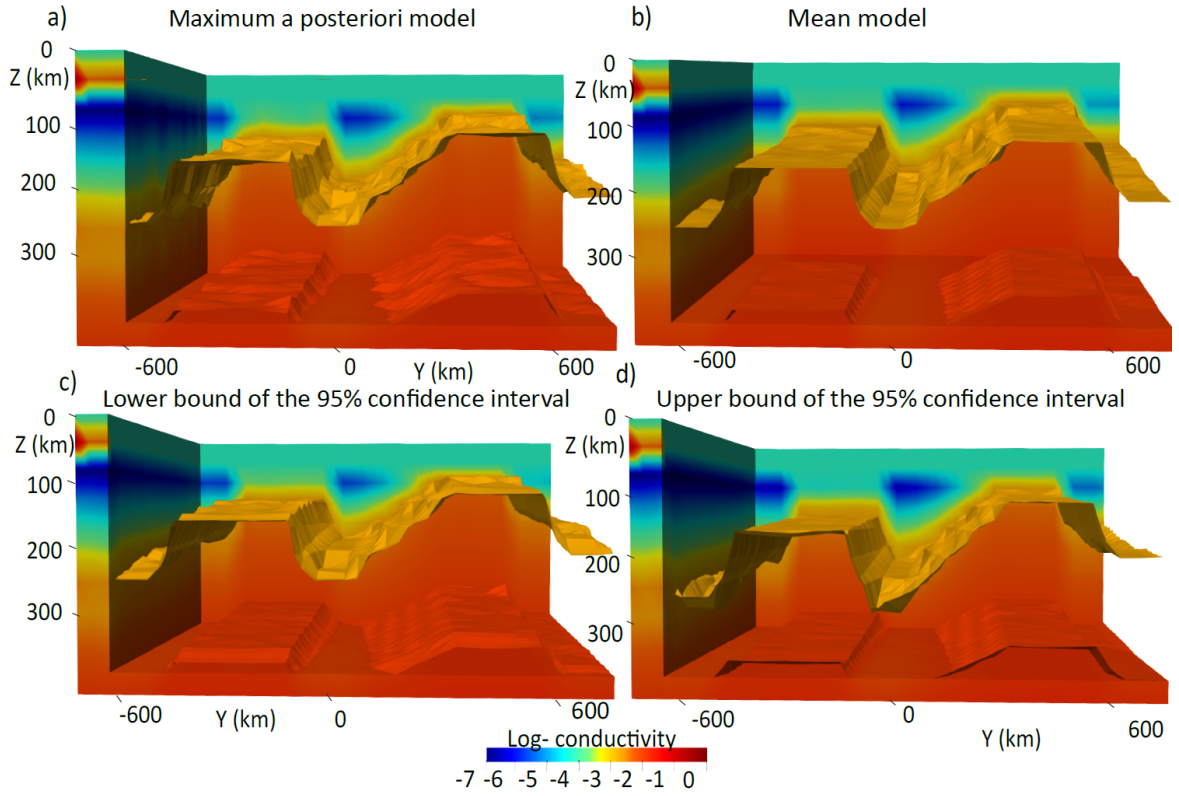


Figure 5. Conductivity structures corresponding to the (a) *maximum a posteriori* (best-fitting) model; (b) mean model; and conductivity models corresponding to the lower (c) and upper bound (d) of the 95% confidence interval of the posterior PDF obtained after 600,000 MCMC steps. The iso-surfaces of -2.8 and $-2 \log_{10}$ S/m are plotted as a reference.

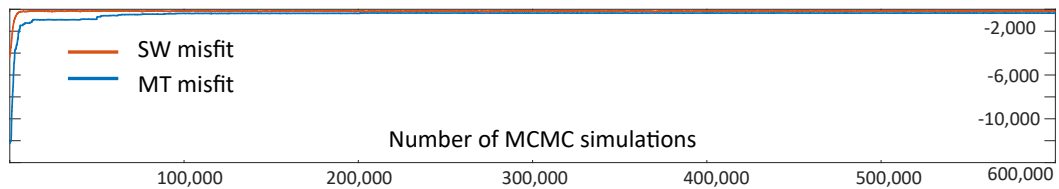


Figure 6. Data misfits for the dispersion curves (red line) and MT (blue line) for each one of the 600,000 RB+MCMC steps.

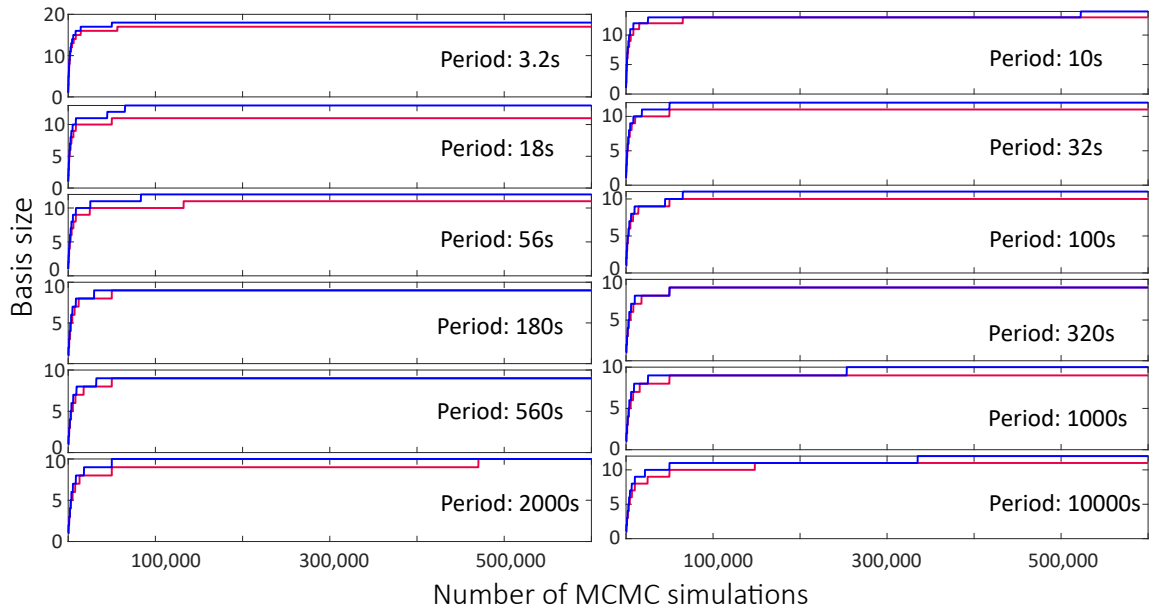


Figure 7. Basis size as a function of the MCMC simulations for different frequencies and field orientations (S_{\perp} mode in blue and S mode in red).

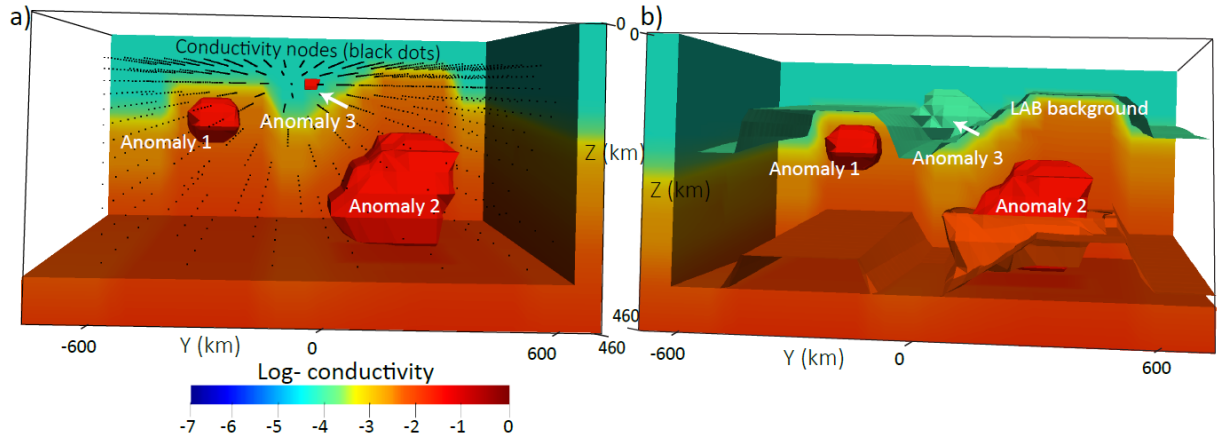


Figure 8. 3D rendering views of the true conductivity structure. Conductivity anomalies are highlighted in both (a) and (b) panels. Black dots in (a) indicate the position of the node-parameters within the inversion volume. Panel (a) shows the iso-surface corresponding to $-1.5 \log_{10}$ (S/m), whereas iso-surfaces of -2.15 , -1.5 and $-4 \log_{10}$ (S/m) are shown in (b).

614 dard deviations of $0.9 \log_{10}(S/m)$. During the fourth stage, we use an adapted multi-
 615 variate log-normal distribution centered on the current sample (see Section 5.4). The start-
 616 ing conductivity model is the same as that used in Example 1 and contains no conduc-
 617 tivity anomalies.

618 The first stage was set to 3,000 steps, where we sample LAB depths one column
 619 at a time. Once the second stage starts, the algorithm randomly decides to sample the
 620 LAB depth of one column or the conductivity values of $n_1 = 2$ nodes. The multivari-
 621 ate proposal for the LAB (start of the third stage) is computed when the chains achieve
 622 250,000 samples and it is adapted every 100,000 LAB samples during the the rest of the
 623 inversion. During this third stage, we propose conductivity values of $n_1 = 2$ random nodes
 624 or LAB depths of $m=6$ random columns (from the adapted multivariate proposal distri-
 625 butions; see Section 5.3). The multivariate log-normal proposal distribution for the
 626 nodes is computed when their chain reaches 400,000 samples (start of the fourth stage)
 627 and it is subsequently adapted every 100,000 steps. During this stage we randomly se-
 628 lect $n_2 = 10$ nodes or $m=6$ columns at a time (see Section 5.4).

629 **6.4.3 Inversion results**

630 We ran a total of 1,000,000 MCMC simulations for 12 frequencies using 2 proces-
 631 sors (Intel(R) Xeon(R) CPU E5-2680 v3 @ 2.50GHz) per frequency. The tolerances used
 632 were $\beta = 0.068$ for the first 150,000 steps and $\beta = 0.058$ for the remaining of the sim-
 633 ulation. Again, even with modest computational resources, the inversion took only 14
 634 days with an average of 1.2 seconds for each simulation. This represents a time reduc-
 635 tion of $\sim 96\%$ for each forward computation. The difference in computational time com-
 636 pared to those presented in our previous paper (Manassero et al., 2020) is due to the cur-
 637 rent implementation of kriging-type interpolation, which is faster and more stable than
 638 the Shepard’s interpolation. We also note that the average time spent in each simula-
 639 tion is higher than those in Example 1. This is mainly due to the higher number of bases
 640 (Fig. 14) required in order to explain the complexity of this 3D model.

641 The MAP and mean models are shown in Figs. 9 together with the 95% confidence
 642 intervals of the posterior PDF. The background conductivity structure and the location
 643 and volume of the conductivity anomalies are well resolved. Depth slices from the 95%
 644 confidence intervals, MAP and mean models are shown in Figs. 10. In this figure we also
 645 include depth slices from five random subsets from the posterior, each obtained as the
 646 mean of 10 randomly chosen models from the entire collection of conductivity models
 647 making up the posterior PDF. As expected, features that are well resolved by the inver-
 648 sion are persistent in all subsets, whereas poorly resolved features show higher variabil-
 649 ity among subsets. The identifiability of the background structure is also illustrated in
 650 Figs. 11 and Figs. S4-S10 of the Supplementary Material, where we show that the true
 651 LAB depths are close to the mean value of the marginal posterior PDFs for all param-
 652 eters. The sizes of the basis per frequency and the SW-MT data misfits for each of the
 653 1,000,000 steps are shown in Figs. 14 and 15, respectively, and show a similar pattern
 654 to those in Fig. 6.

655 It is worth noting that contrary to what we would expect from an inversion of MT
 656 data alone (see results in e.g. Manassero et al., 2020; Rosas-Carbajal et al., 2013), model
 657 variability decreases with depth. The reason for this is the tighter constraints that the
 658 SW data puts on the background thermochemical structure. Compared with the results
 659 presented in Manassero et al. (2020), the joint inversion of MT with SW data highly re-
 660 duces model uncertainty and increases model resolution.

661 Examples of the posterior PDFs of SW and MT data are shown in Figs. 12 and
 662 13; additional posterior PDFs are shown in the Supplementary Material. All of the dis-
 663 persion data points are contained within one standard deviation of the posterior PDFs.
 664 This is also the case for the great majority of the MT data, although a poor data fit (or

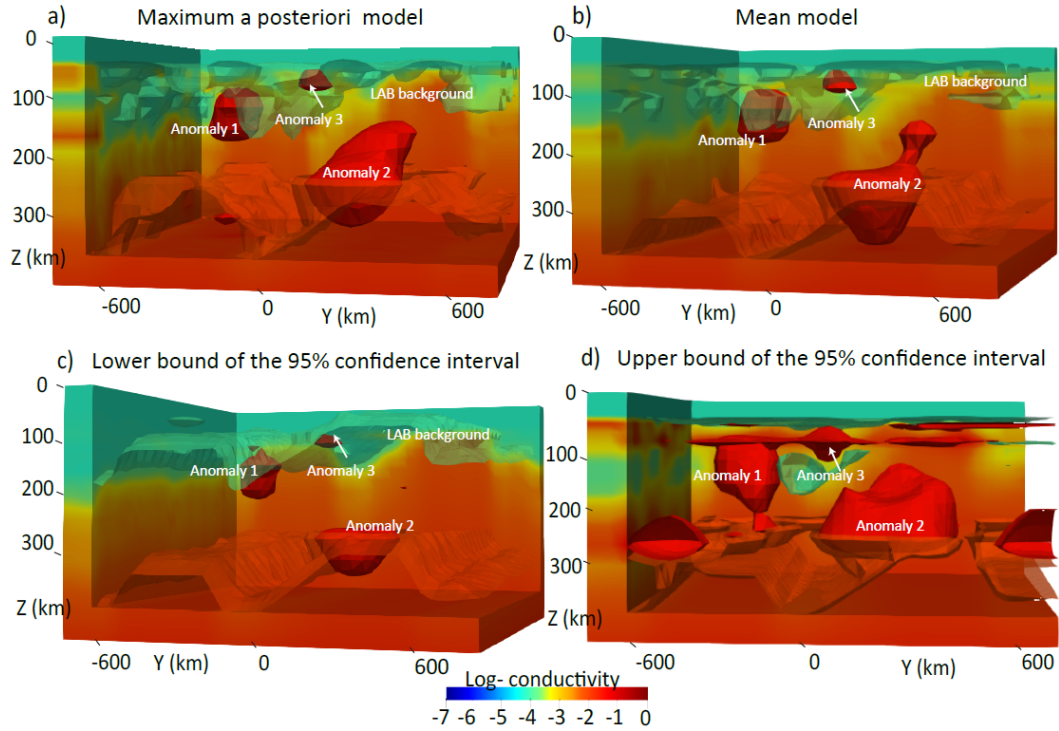


Figure 9. 3D rendering views of the conductivity structure corresponding to the (a) *maximum a posteriori* model; (b) mean model; (c) lower and (d) upper bound of the 95% confidence interval of the posterior PDF obtained after 1,000,000 MCMC steps. The iso-surfaces of -1.5 , -2.15 and $-4 \log_{10} \text{ S/m}$ are plotted as a reference. The background structure and the conductivity anomalies are highlighted in all panels.

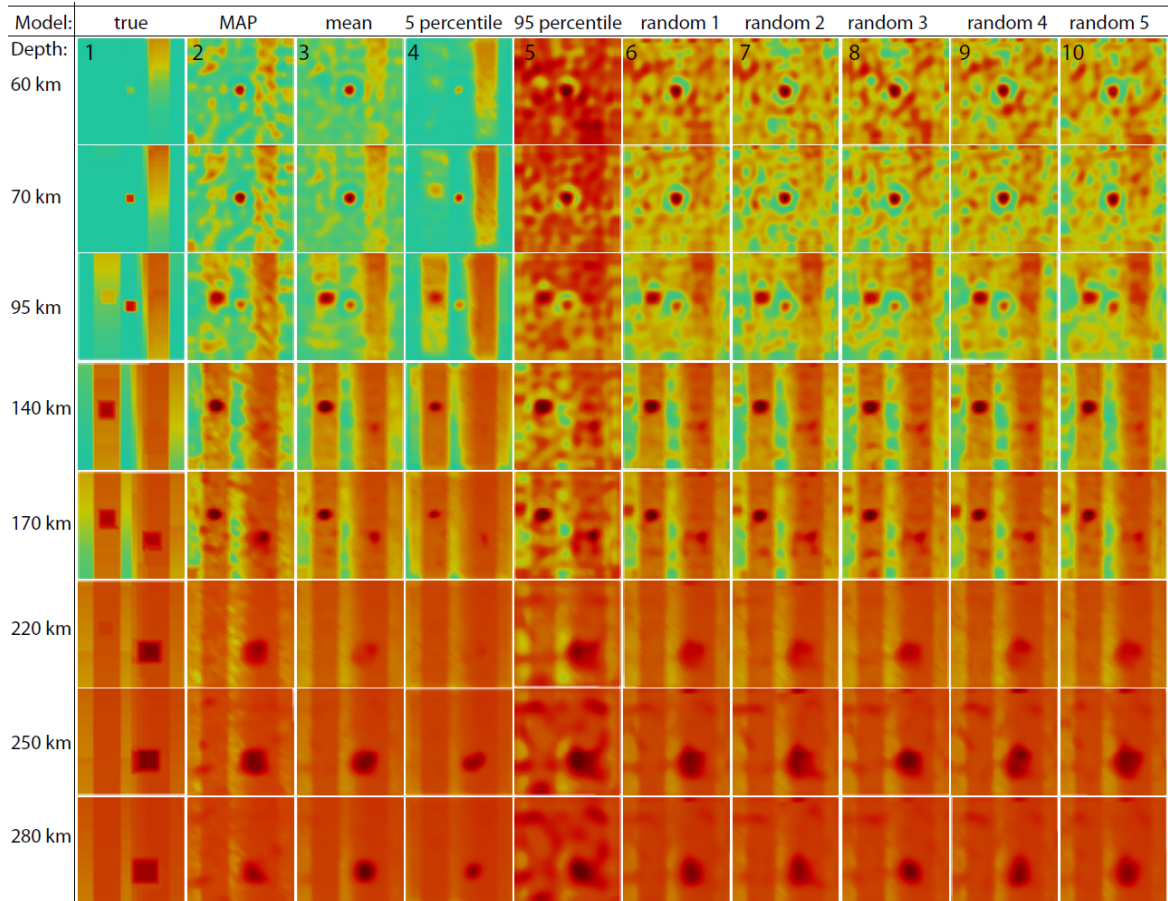


Figure 10. Columns (1)-(5): depth slices from the (1) true model; (2) MAP model, (3) mean and conductivity models corresponding to (4) the 5% percentile and (5) the 95% percentile of the posterior PDF. Columns (6)-(10): depth slices for five mean models computed with 10 random samples of the posterior PDF. Selected depths are shown on the left of the figure.

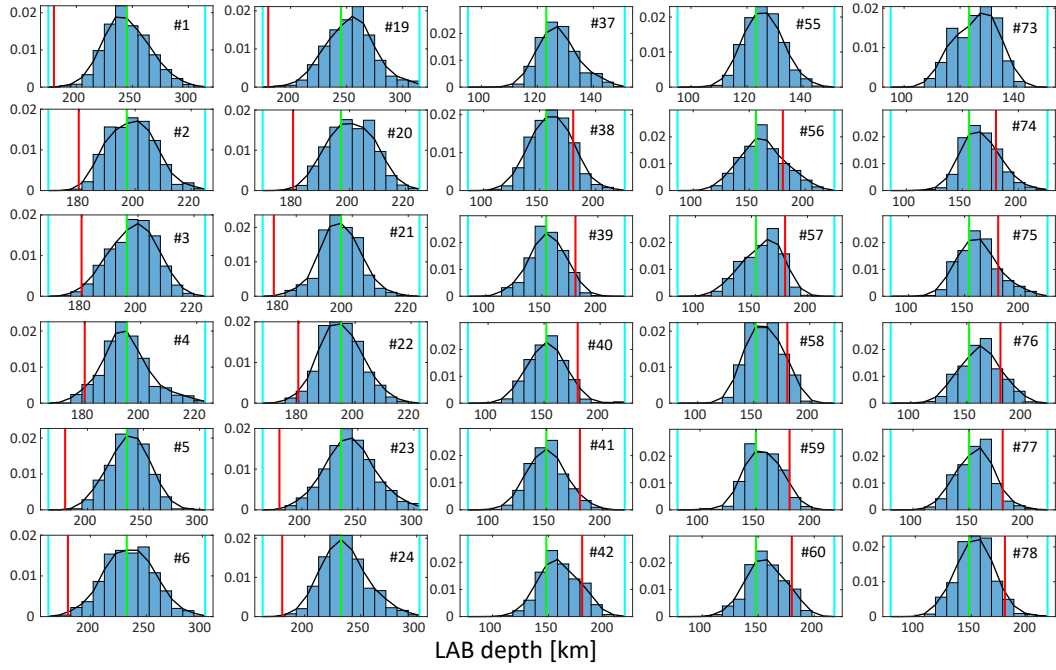


Figure 11. Marginal posterior PDFs (blue bars) of 30 LAB depths obtained after 1,000,000 RB+MCMC steps. The real value, starting value and prior bounds of each parameter are shown in green, red, and light blue vertical lines, respectively. The best Gaussian fits to the real PDFs given by the histograms are shown in black lines. The numbers within each panel correspond to the columns highlighted in Fig. 1.b.

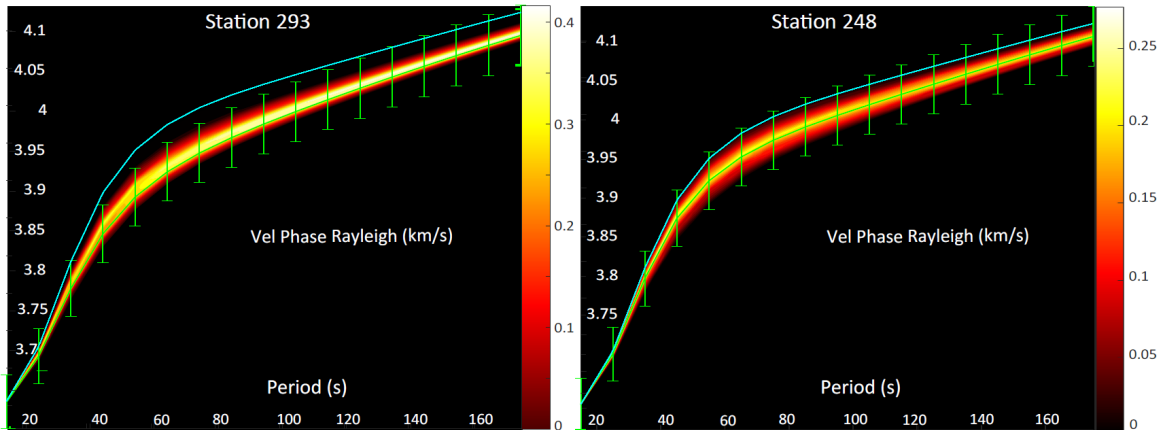


Figure 12. Posterior PDFs of Rayleigh dispersion curves for stations (a) 293 and (b) 248. Synthetic data and error bars are plotted in green and the computed data for the initial model is plotted in blue. The location of the stations are shown in Fig. 1.a.

665 bias) is observed in some stations. As mentioned in Section 6.1, the MT synthetic data
 666 is computed with the true conductivity model (Fig. 8), whereas the conductivity mod-
 667 els used in the actual inversion are derived from the interpolation of nodal values. This
 668 discrepancy or inadequacy between models is the main reason of the poorer data fit seen
 669 at some stations (e.g. Smith, 2013).

670 The results from this example demonstrate that the joint probabilistic inversion
 671 of wave dispersion and MT data i) is a practical option with modest computational re-
 672 sources, ii) succeeded in identifying the true LAB and conductivity structures (background
 673 plus anomalies) and iii) produced well behaved posterior distributions and global mea-
 674 sures of uncertainty and correlations between model parameters. In addition, when
 675 compared to the results in Manassero et al. (2020) for the inversion of MT alone, the cur-
 676 rent joint inversion provides better resolution to both the background and anomalies.

677 7 Discussion

678 Here we discuss some practical aspects relevant to real inversions and possible tech-
 679 nical improvements of the algorithm.

680 7.1 Inverting for Crustal Structure and Bulk Mantle Composition

681 Since our main interest is the deep lithospheric structure, we have so far assumed
 682 constant properties and thickness for the crust. This is similar to assuming that we have
 683 good prior information, for example, from a previous deterministic inversion or from pre-
 684 vious independent studies. A similar idea was applied to a real joint inversion by Jones
 685 et al. (2017). However, if the interest is also in the shallow crust, we could simply dis-
 686 cretize the crust with layers of constant properties (e.g. bulk density, V_s , V_p and σ) within
 687 each 1D column and include them in the vector of model parameters. Perhaps a more
 688 efficient possibility is to define crustal nodes with associated σ , density, V_s , and V_p
 689 and interpolate these values to each numerical cell within the crust, similar to what we do
 690 in the mantle for σ . We are currently working on these schemes and results will be pre-
 691 sented in a forthcoming publication.

692 Throughout this work we have also considered a constant major-element compo-
 693 sition in the mantle. In practical applications with emphasis on the general structure of

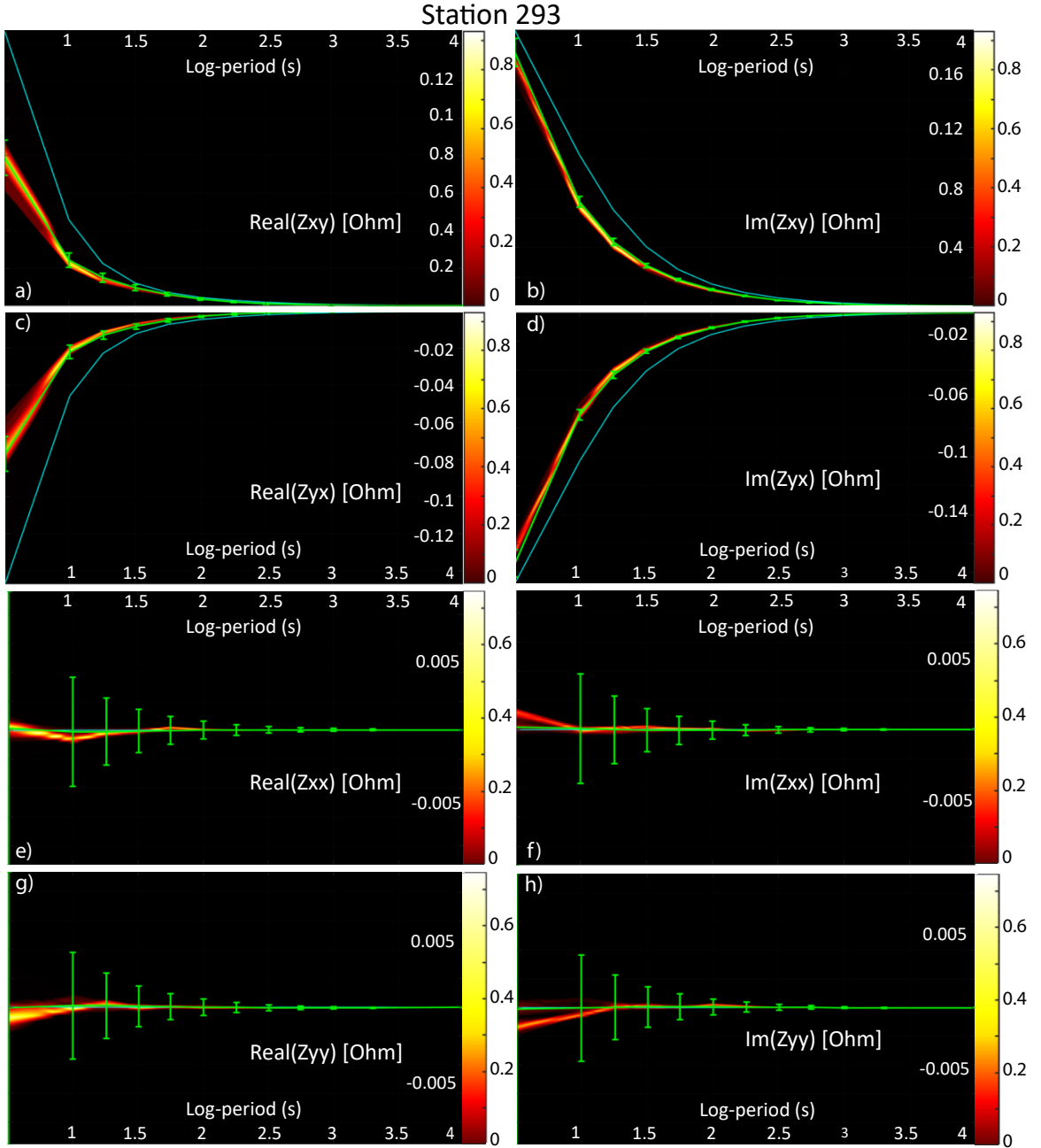


Figure 13. Posterior PDFs of MT data for station 293. Synthetic data and error bars are plotted in green and the computed data for the initial model is plotted in blue. (a)-(d) Posterior PDFs of the real and imaginary parts of the off-diagonal components of the impedance tensor. (e)-(h) Posterior PDFs of the real and imaginary parts of the diagonal components. The location of the station is shown in Fig. 1.a.

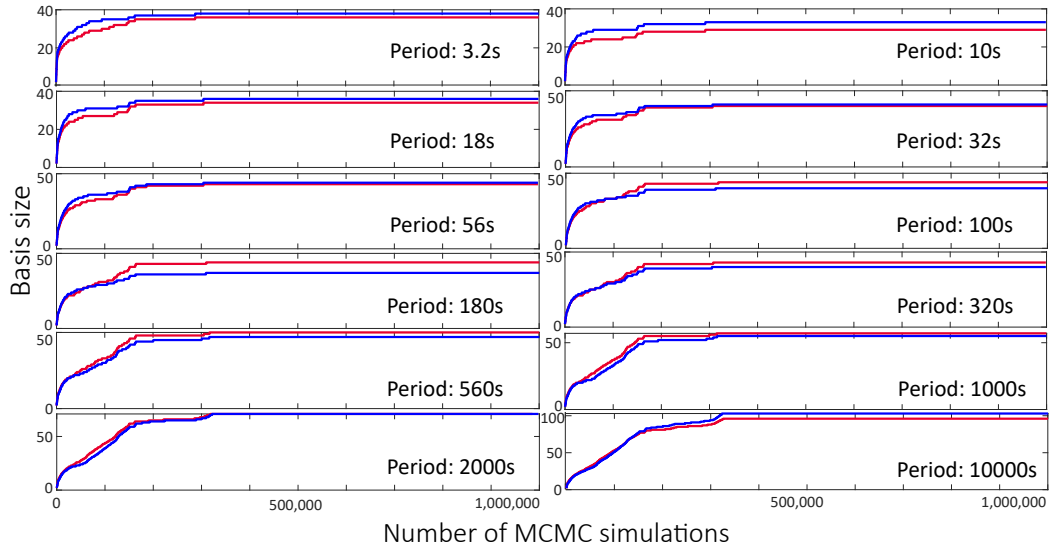


Figure 14. Basis size as a function of the RB+MCMC steps for different frequencies and field orientations (S_{\perp} mode in blue, and S mode in red).

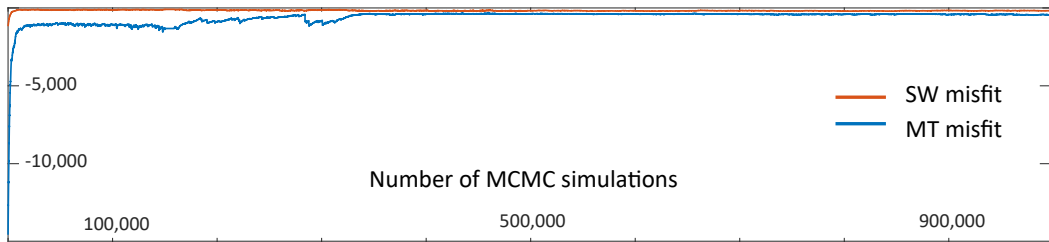


Figure 15. Data misfits for the dispersion curves (red line) and MT (blue line) for each of the 1,500,000 RB+MCMC steps.

694 the lithosphere/upper mantle, this is not a major issue. This is because the sensitivity
 695 to bulk major-element composition is of second-order compared to other factors such as
 696 temperature and fluid content. Moreover, in order to increase the sensitivity to bulk man-
 697 tle composition, the inclusion of gravity and/or geoid anomalies into the inversion be-
 698 comes a requirement (J. Afonso et al., 2013a; J. C. Afonso et al., 2013b; J. C. Afonso,
 699 Rawlinson, et al., 2016). This is left for future work.

700 7.2 Parameterization and Efficiency of the Algorithm

701 The current parameterization is specifically tailored to constrain the first-order con-
 702 ductivity background and to locally accommodate smaller-scale anomalies. This param-
 703 eterization also allows for considerable model variance/flexibility, as it is capable of ap-
 704 proximating any conductivity structure, and it favors a rapid convergence at the begin-
 705 ning of the inversion. There are, however, two main drawbacks: i) it is almost impos-
 706 sible to know a priori the minimum number of parameters necessary to retrieve the true
 707 model; ii) the algorithm can be inefficient if the number and location of the nodes are
 708 not optimal, as an over-parameterization of the model can seriously compromise the con-
 709 vergence of the MCMC algorithm, whereas an under-paramaterization can introduce spu-
 710 rious features in regions where the conductivity nodes are far from each other (since the
 711 kriging-like interpolation produces unreal values where poor or none information from
 712 the surrounding nodes is available; see Appendix B and B1).

713 In practice, these issues are addressed by running preliminary inversions (similar
 714 to what is done in deterministic inversions with the variance-resolution trade-off diagram;
 715 Menke (2018)). A more efficient approach would be to implement trans-dimensional al-
 716 gorithms (e.g. Ray & Myer, 2019; Brodie & Jiang, 2018; Bodin & Sambridge, 2009) to
 717 identify the minimum dimensionality of the model (i.e. parsimony), as required by the
 718 data. In particular, the combination of the kriging interpolation (also known as Gaus-
 719 sian process regression) with a trans-dimensional algorithm is a promising approach to
 720 tackle the problem of potential under/over-parameterization (e.g. Ray & Myer, 2019).

721 7.3 Ergodicity of the Algorithm

722 While the sampling strategy described in Section 5 brings in a number of impor-
 723 tant benefits to the joint RB+MCMC inversion, the first stage (with focus on constrain-
 724 ing the first-order temperature structure) can potentially affect the ergodicity of the chain.
 725 Given that we deliberately chose to sample one set of parameters (i.e. the LAB depths)
 726 for a pre-defined number of MCMC steps, the chain is precluded from reaching the states
 727 of the first stage once the second stage starts (i.e. it is not irreducible). As demonstrated
 728 in the examples, only a small number of iterations are necessary in the first stage for the
 729 LAB's chains to approach the high-probability region of the posterior PDFs. We there-
 730 fore note that a sufficient condition to ensure the overall ergodicity (e.g. Meyn & Tweedie,
 731 2012) and correct convergence of the sampler requires the *burn-in* period to be larger
 732 than the total number of steps in the first stage (*LAB-stage*).

733 8 Conclusions

734 We presented a novel, MCMC-driven probabilistic joint inversion of 3D magnetotel-
 735 luric (MT) and surface-wave (SW) dispersion data for imaging the electrical conductiv-
 736 ity and velocity structures of the whole lithosphere and sublithospheric upper mantle.
 737 The method is based on i) an efficient parallel-in-parallel structure to solve the 3D MT
 738 forward problem, ii) the combination of a reduced order, MCMC-driven strategy to com-
 739 pute fast and accurate surrogate solutions to the 3D MT forward problem, iii) adaptive
 740 strategies for both the MCMC algorithm and the surrogate and iv) an efficient dual pa-
 741 rameterization to couple both data sets.

742 The feasibility, potential and efficiency of our algorithm to solve the joint inverse
 743 problem are demonstrated with two realistic whole-lithosphere examples. In both cases,
 744 we obtain staggering gains in computational efficiency (>96%) compared to a traditional
 745 MCMC implementation. Average times per MCMC step are of the order of 1 sec, even
 746 when using modest computational resources. We also show that the inclusion of SW data
 747 and a simple Cascade-Metropolis algorithm resulted in drastic improvements in compu-
 748 tational efficiency and quality of the recovered models compared to the RB+MCMC in-
 749 version of MT data only (Manassero et al., 2020).

750 The model parameterization takes advantage of the differential sensitivities of MT
 751 and SW dispersion data to different aspects of the problem by using two sets of param-
 752 eters. The first set corresponds to LAB depths, which control the large-scale (background)
 753 conductivity/velocity structure. The second set corresponds to conductivity nodes in-
 754 side the model, which control the small-scale conductivity anomalies. An additional ad-
 755 vantage of using this parameterization is that a rapid convergence is achieved by using
 756 the LAB depths to constrain the first-order conductivity/velocity background at the be-
 757 ginning of the inversion. Once this first-order convergence has been achieved, the nodes
 758 are used to locally modify the background to fit the smaller-scale features of the data.

759 Finally, we note that proposed method is general enough to incorporate more ad-
 760 vanced MCMC algorithms (e.g. tras-dimensional schemes, parallel tempering, differen-
 761 tial evolution), additional model parameters (e.g. bulk mantle composition) and other
 762 forward operators (e.g. gravity anomalies).

763 Appendix A Mapping Thermochemical Parameters to Electrical Con- 764 ductivity

The temperature dependence of electrical conductivity can be described with an Arrhenius-type Equation:

$$\sigma = \sigma_0 \exp\left(\frac{-\Delta H}{k_B T}\right), \quad (\text{A1})$$

765 where σ_0 is the so-called pre-exponential factor, T [K] is absolute temperature and k_B
 766 [eV/K] the Boltzmann's constant. ΔH [eV] is the pressure-dependent activation enthalpy,
 767 defined as

$$\Delta H = \Delta E + P\Delta V, \quad (\text{A2})$$

768 where P is the pressure [GPa], ΔE and ΔV are the activation energy and activation vol-
 769 ume, respectively.

770 The main bulk conduction mechanisms in mantle minerals are ionic conduction,
 771 small polaron (hopping) conduction and proton conduction (e.g. Yoshino, 2010). Each
 772 mechanism follows an Arrhenius-type equation with particular activation energies de-
 773 pending on their charge mobility. These three conduction mechanisms can be integrated
 774 in a model for the electrical conductivity of mantle rocks as a function of pressure, tem-
 775 perature, water content, and composition (via Fe content) for each mineral phase (see
 776 also Yoshino et al., 2009; Fullea et al., 2011):

$$\sigma = \sigma_0 \exp\left(\frac{-\Delta H(X_{Fe}, P)}{k_B T}\right) + \sigma_{0i} \exp\left(\frac{-\Delta H_i}{k_B T}\right) + \sigma_p \quad (\text{A3a})$$

$$\sigma_p = f(C_w) \exp\left(\frac{-\Delta H_{wet}(C_w)}{k_B T}\right), \quad (\text{A3b})$$

$$-\Delta H(X_{Fe}, P) = a + bX_{Fe} + cX_{Fe}^2 + dX_{Fe}^3 + eX_{Fe}^4 + fX_{Fe}^5 + P\Delta V, \quad (\text{A3c})$$

Table A1: Parameters used to compute mantle conductivity

Phase	σ_0	σ_{0i}	a	b	c	d	e	f	ΔV	ΔH_i	X_{Fe}
Olivine	2.70	4.73	1.64	0.246	-4.85	3.26			0.68	2.31	0.10
Opx	3.0		1.90	-2.77	2.61	-1.09					0.107
Cpx	3.25		2.07	-2.77	2.61	-1.09					$5.84e^{-2}$
Garnet		4.96	2.60	-15.33	80.40	-194.6	202.6	-75.0			0.168

777 where σ_0 , σ_{0i} [S/m] and $f(C_w)$ are the small polaron, ionic and proton pre-exponential
778 factors, respectively, ΔV [cm^3/mol] is activation volume, ΔH , ΔH_i [eV] and ΔH_{wet} are
779 activation enthalpies and X_{Fe} is the bulk Fe content in wt%.

780 The first term in the right-hand side of Equation A3a describes the contribution
781 from small polaron conduction. As mentioned above, the activation enthalpy for this pro-
782 cess depends on the iron content and pressure. This dependence is represented by a poly-
783 nomial on X_{Fe} (Eq. A3c) plus a term that depends on pressure (the coefficients a, b, c, d, e, f
784 are determined experimentally). The second term of Equation A3a represents ionic con-
785 duction at high temperature and the third term (σ_p) represents the proton conduction
786 due to the presence of “water” (hydrogen diffusion). $f(C_w)$ and ΔH_{wet} are functions of
787 the water content C_w [wt%] and they are obtained from laboratory experiments. The
788 reader is referred to Fullea et al. (2011) and Pommier (2014) for a summary on results
789 from different laboratories.

790 Appendix B Kriging Interpolation

Kriging, or Gaussian process regression, is one of the most common methods for
spatial interpolation (see e.g. Cressie, 1993; Rasmussen, 1997; Williams & Rasmussen,
1996; Omre, 1987; M. Gibbs & MacKay, 1997; M. N. Gibbs, 1998). The main idea is to
predict (or interpolate) the value of a function Z at m locations from n observations by
computing average spatial weights (W). In simple kriging, these weights are derived us-
ing a known covariance function c between observations (given by the matrix K_{obs}) and
between the observations and the m estimation locations (given by the covariance ma-
trix K_{loc}):

$$W = K_{obs}^{-1} \cdot K_{loc}, \quad (B1)$$

791 where $K_{obs} = \begin{pmatrix} c(x_1^{obs}, x_1^{obs}) & \dots & c(x_1^{obs}, x_n^{obs}) \\ \dots & \dots & \dots \\ c(x_n^{obs}, x_1^{obs}) & \dots & c(x_n^{obs}, x_n^{obs}) \end{pmatrix}$ and $K_{loc} = \begin{pmatrix} c(x_1^{obs}, x_1^{loc}) & \dots & c(x_1^{obs}, x_m^{loc}) \\ \dots & \dots & \dots \\ c(x_n^{obs}, x_1^{loc}) & \dots & c(x_n^{obs}, x_m^{loc}) \end{pmatrix}$.

793 The interpolation (or estimated value) at the m locations is then given by $Z^{loc} =$
794 $W \cdot Z^{obs}$, where Z^{obs} is the vector containing the n observations.

The covariance function c can take any form with the only constrain that it must
generate a non-negative definite covariance matrix. A common form is given by (e.g. M. Gibbs
& MacKay, 1997):

$$c(\mathbf{x}_m, \mathbf{x}_n) = \theta_1 \exp\left(-\frac{1}{2} \sum_l \frac{(x_m^l - x_n^l)^2}{r_l^2}\right) + \theta_2, \quad (B2)$$

795 where x_n^l is the l component of \mathbf{x}_n . θ_1 and θ_2 are hyperparameters, where θ_1 represents
796 the overall vertical scale relative to the mean field and θ_2 gives the vertical uncertainty.

797 r_l is the correlation or scale length and it characterizes the distance in the direction l
 798 over which the value of Z varies significantly. It should be noted that since the spatial
 799 weights (W) depends on the covariance function c , the interpolated values at the m lo-
 800 cations also depends on the chosen form for c .

801 **B1 Spatially varying length scales**

802 The covariance function of Eq. B2 assumes that the correlation length (r_l) is fixed
 803 in each direction (l) and location (\mathbf{x}). In the most general case, however, assuming a fixed
 804 r_l might lead to a simplistic and poor representation of the conductivity model. We, there-
 805 fore, use a positive definite covariance function with spatially variable correlation lengths
 806 (M. Gibbs & MacKay, 1997; M. N. Gibbs, 1998):

$$c(\mathbf{x}_m, \mathbf{x}_n) = \theta_1 \prod_l \left(\frac{2r_l(\mathbf{x}_m)r_l(\mathbf{x}_n)}{r_l^2(\mathbf{x}_m) + r_l^2(\mathbf{x}_n)} \right)^{1/2} \exp\left(- \sum_l \frac{(x_m^l - x_n^l)^2}{r_l^2(\mathbf{x}_m) + r_l^2(\mathbf{x}_n)} \right) \quad (\text{B3})$$

807 where $r_l(\mathbf{x})$ is an arbitrary parameterized function of position \mathbf{x} defined in $[-1, 1]^2 \times [0, 1]$.
 808 The form of $r_l(\mathbf{x})$ as a function of the scaled coordinates (x, y, z) used in Examples 1 and
 809 2 in the main text is shown in Procedure 1. This covariance function has the property
 810 that the variance is independent of \mathbf{x} and equal to θ_1 . Since a change in θ_1 will produce
 811 changes in the vertical scale in the whole domain (see previous section), the inclusion
 812 of θ_1 as an additional parameter of the inversion can (potentially) benefit the efficiency
 813 and convergence of the algorithm. The implementation of θ_1 as an hyper-parameter of
 814 the inversion is left for future work.

815 **Appendix C Log-normal proposal distributions**

816 The log-normal distribution (Gaussian in log-scale) used in the second stage is de-
 817 fined as:

$$y(m_t^i) = \frac{1}{\sqrt{2\pi m_t^i s}} \exp\left(-\frac{\ln(m_t^i) - \mu}{2s^2} \right)^2, \quad (\text{C1})$$

818 where $y(m_t^i)$ is the proposed value for node i , and μ and s are the mean and standard
 819 deviation in log-scale.

820 In Section 5 we have chosen to define a multivariate Gaussian proposal of dimen-
 821 sion $N_{nodes} \times N_{nodes}$, where N_{nodes} is the number of conductivity nodes in the model. Since
 822 the nodes' conductivity values can span several orders of magnitude, the Gaussian pro-
 823 posal is defined in log-scale but we evaluate its probability $q(\cdot)$ in linear scale, i.e. a mul-
 824 tivariate log-normal PDF centered at the current state \mathbf{m}_{t-1} with covariance Σ :

$$q(\mathbf{m}_t | \mathbf{m}_{t-1}) = \frac{1}{(2\pi)^{\frac{N_{nodes}}{2}} (\det \Sigma)^{\frac{1}{2}} \prod_{j=1}^{N_{nodes}} m_t^j} \exp\left[-\frac{1}{2} (\ln(\mathbf{m}_t) - \ln(\mathbf{m}_{t-1}))^t \Sigma^{-1} (\ln(\mathbf{m}_t) - \ln(\mathbf{m}_{t-1})) \right], \quad (\text{C2})$$

825 where \mathbf{m}_t is the proposed value for all nodes and \mathbf{m}_{t-1} is the current sample.

Algorithm 1 Definition of $r_l(\mathbf{x})$ as a function of the scaled coordinates (x, y, z) .

```

procedure  $r_l(x)$ 
  if  $z \geq 0.9$  then
     $r_3 = 0.5$ 
     $r_2 = r_1 = 0.4$ 
  else if  $z < 0.9$  and  $z \geq 0.8$  then
     $r_3 = 0.45$ 
     $r_2 = r_1 = 0.35$ 
  else if  $z < 0.8$  and  $z \geq 0.7$  then
     $r_3 = 0.4$ 
     $r_2 = r_1 = 0.3$ 
  else if  $z < 0.7$  and  $z \geq 0.6$  then
     $r_3 = 0.38$ 
     $r_2 = r_1 = 0.28$ 
  else if  $z < 0.6$  and  $z \geq 0.5$  then
     $r_3 = 0.35$ 
     $r_2 = r_1 = 0.25$ 
  else if  $z < 0.5$  and  $z \geq 0.4$  then
     $r_3 = 0.33$ 
     $r_2 = r_1 = 0.23$ 
  else if  $z < 0.4$  and  $z \geq 0.3$  then
     $r_3 = 0.3$ 
     $r_2 = r_1 = 0.2$ 
  else if  $z < 0.34$  and  $z \geq 0.2$  then
     $r_3 = 0.28$ 
     $r_2 = r_1 = 0.2$ 
  else if  $z < 0.2$  then
     $r_3 = 0.2$ 
     $r_2 = r_1 = 0.18$ 
  end if
end procedure

```

Acknowledgments

We thank Farshad Salajegheh for providing part of his Matlab codes for plotting results. Special thanks to Kate Selway and Anandaroop Ray for their suggestions at different stages of this work. The 3D rendering views were created using ParaView (Ahrens et al., 2005).

MCM thanks support from an International Macquarie Research Excellence Scholarship (iMQRES). MCM and JCA acknowledge support from ARC Grant DP160103502, ARC Linkage Grant LP170100233, the ARC Centre of Excellence Core to Crust Fluids Systems (<http://www.ccfs.mq.edu.au>) and the Centre for Earth Evolution and Dynamics, Geoscience Australia and the European Space Agency via the “3D Earth - A Dynamic Living Planet”. FZ acknowledges support from CONICET through grant PIP 112-201501-00192. SZ has been funded by the Spanish Ministry through grant DPI2017-85139-C2-2-R, by Catalan government through grant 2017-SGR-1278 and by the EU’s Horizon 2020 research and innovation programme under the Marie Skłodowska-Curie grant agreement No 777778.

References

- Afonso, J., Fullea, J., Griffin, W., Yang, Y., Jones, A., Connolly, J., & O’Reilly, S. (2013a). 3-D multiobservable probabilistic inversion for the compositional and thermal structure of the lithosphere and upper mantle. I: A priori petrological information and geophysical observables. *Journal of Geophysical Research: Solid Earth*, *118*(5), 2586–2617.
- Afonso, J. C., Fernandez, M., Ranalli, G., Griffin, W., & Connolly, J. (2008). Integrated geophysical-petrological modeling of the lithosphere and sublithospheric upper mantle: Methodology and applications. *Geochemistry, Geophysics, Geosystems*, *9*(5).
- Afonso, J. C., Fullea, J., Yang, Y., Connolly, J., & Jones, A. (2013b). 3-D multiobservable probabilistic inversion for the compositional and thermal structure of the lithosphere and upper mantle. II: General methodology and resolution analysis. *Journal of Geophysical Research: Solid Earth*, *118*(4), 1650–1676.
- Afonso, J. C., Moorkamp, M., & Fullea, J. (2016). Imaging the lithosphere and upper mantle: Where we are at and where we are going. In N. L. M. Moorkamp, P. Lelievre & A. Khan (Eds.), *Integrated imaging of the earth: Theory and applications* (pp. 191–218). John Wiley & Sons.
- Afonso, J. C., Ranalli, G., & Fernández, M. (2005). Thermal expansivity and elastic properties of the lithospheric mantle: results from mineral physics of composites. *Physics of the Earth and Planetary Interiors*, *149*(3-4), 279–306.
- Afonso, J. C., Ranalli, G., Fernández, M., Griffin, W. L., O’Reilly, S. Y., & Faul, U. (2010). On the V_p/V_s -Mg# correlation in mantle peridotites: Implications for the identification of thermal and compositional anomalies in the upper mantle. *Earth and Planetary Science Letters*, *289*(3-4), 606–618.
- Afonso, J. C., Rawlinson, N., Yang, Y., Schutt, D. L., Jones, A. G., Fullea, J., & Griffin, W. L. (2016). 3-D multiobservable probabilistic inversion for the compositional and thermal structure of the lithosphere and upper mantle: III. Thermochemical tomography in the Western-Central US. *Journal of Geophysical Research: Solid Earth*, *121*(10), 7337–7370.
- Ahrens, J., Geveci, B., & Law, C. (2005). Paraview: An end-user tool for large data visualization. *The visualization handbook*, 717–731.
- Amestoy, P. R., Duff, I. S., L’Excellent, J.-Y., & Koster, J. (2001). A fully asynchronous multifrontal solver using distributed dynamic scheduling. *SIAM Journal on Matrix Analysis and Applications*, *23*(1), 15–41.
- Amestoy, P. R., Guermouche, A., L’Excellent, J.-Y., & Pralet, S. (2006). Hybrid scheduling for the parallel solution of linear systems. *Parallel computing*, *32*(2),

- 878 136–156.
- 879 Bennington, N. L., Zhang, H., Thurber, C. H., & Bedrosian, P. A. (2015). Joint
880 inversion of seismic and magnetotelluric data in the Parkfield Region of California
881 using the normalized cross-gradient constraint. *Pure and Applied Geophysics*,
882 *172*(5), 1033–1052.
- 883 Birch, F. (1961). Composition of the earth’s mantle. *Geophysical Journal Interna-*
884 *tional*, *4*(Supplement.1), 295–311.
- 885 Birch, F. (1964). Density and composition of mantle and core. *Journal of geophysical*
886 *research*, *69*(20), 4377–4388.
- 887 Bodin, T., & Sambridge, M. (2009). Seismic tomography with the reversible jump
888 algorithm. *Geophysical Journal International*, *178*(3), 1411–1436.
- 889 Bosch, M. (1999). Lithologic tomography: From plural geophysical data to lithology
890 estimation. *Journal of Geophysical Research: Solid Earth*, *104*(B1), 749–766.
- 891 Brodie, R., & Jiang, W. (2018). Trans-dimensional Monte Carlo inversion of short
892 period magnetotelluric data for cover thickness estimation. *ASEG Extended Ab-*
893 *stracts*, *2018*(1), 1–7.
- 894 Calvetti, D., & Somersalo, E. (2007). *An introduction to Bayesian scientific com-*
895 *puting: ten lectures on subjective computing* (Vol. 2). Springer Science & Business
896 Media.
- 897 Christen, J. A., & Fox, C. (2005). Markov chain Monte Carlo using an approxima-
898 tion. *Journal of Computational and Graphical statistics*, *14*(4), 795–810.
- 899 Conrad, P. R., Marzouk, Y. M., Pillai, N. S., & Smith, A. (2016). Accelerat-
900 ing asymptotically exact MCMC for computationally intensive models via local
901 approximations. *Journal of the American Statistical Association*, *111*(516), 1591–
902 1607.
- 903 Cressie, N. (1993). *Statistics for spatial data* (Revised Edition ed.). Wiley-
904 Interscience.
- 905 Cui, T., Marzouk, Y. M., & Willcox, K. E. (2015). Data-driven model reduction
906 for the Bayesian solution of inverse problems. *International Journal for Numerical*
907 *Methods in Engineering*, *102*(5), 966–990.
- 908 Douglas Jr, J., Santos, J. E., & Sheen, D. (2000). A nonconforming mixed finite el-
909 ement method for Maxwell’s Equations. *Mathematical Models and Methods in Ap-*
910 *plied Sciences*, *10*(04), 593–613.
- 911 Douglas Jr, J., Santos, J. E., Sheen, D., & Ye, X. (1999). Nonconforming galerkin
912 methods based on quadrilateral elements for second order elliptic problems.
913 *ESAIM: Mathematical Modelling and Numerical Analysis*, *33*(4), 747–770.
- 914 Evans, R. (2012). Conductivity of Earth materials. In J. A. Chave A. (Ed.), *The*
915 *magnetotelluric method, theory and practice* (pp. 50–95). Cambridge: Cambridge
916 Univ. Press New York.
- 917 Evans, R. L., Benoit, M. H., Long, M. D., Elsenbeck, J., Ford, H. A., Zhu, J., &
918 Garcia, X. (2019). Thin lithosphere beneath the central Appalachian Mountains:
919 A combined seismic and magnetotelluric study. *Earth and Planetary Science*
920 *Letters*, *519*, 308–316.
- 921 Feng, R., Yan, H., & Zhang, R. (1986). Fast inversion method and corresponding
922 programming for 3d potential field. *Acta Geol Sin*, *4*(3), 390–402.
- 923 Florentin, E., & Díez, P. (2012). Adaptive reduced basis strategy based on goal ori-
924 ented error assessment for stochastic problems. *Computer Methods in Applied Me-*
925 *chanics and Engineering*, *225*, 116–127.
- 926 Frangos, M., Marzouk, Y., Willcox, K., & van Bloemen Waanders,
927 B. (2011). Surrogate and reduced-order modeling: a compari-
928 son of approaches for large-scale statistical inverse problems. In
929 O. G. M. H. D. K. B. M. Y. M. L. T. B. v. B. W. L. Biegler G. Biros & K. Will-
930 cox (Eds.), *Computational methods for large-scale inverse problems and quantifica-*
931 *tion of uncertainty* (p. 266–290). John Wiley & Sons.

- 932 Fullea, J., Muller, M., & Jones, A. (2011). Electrical conductivity of conti-
 933 nental lithospheric mantle from integrated geophysical and petrological mod-
 934 eling: Application to the Kaapvaal Craton and Rehoboth Terrane, southern
 935 Africa. *Journal of Geophysical Research: Solid Earth*, *116*(B10), 94–105. doi:
 936 doi:10.1029/2011JB008544
- 937 Galabert, O., Zlotnik, S., Afonso, J. C., & Diez, P. (2019). Ultra-fast Stokes flow
 938 solvers for geophysical-geodynamic inverse problems and sensitivity analyses based
 939 on reduced order modeling. *Manuscript in review*.
- 940 Gallardo, L. A., & Meju, M. A. (2007). Joint two-dimensional cross-gradient imag-
 941 ing of magnetotelluric and seismic travelttime data for structural and lithological
 942 classification. *Geophysical Journal International*, *169*(3), 1261–1272.
- 943 Gibbs, M., & MacKay, D. J. (1997). Efficient implementation of gaussian processes.
 944 Gibbs, M. N. (1998). *Bayesian gaussian processes for regression and classification*
 945 (Unpublished doctoral dissertation). Citeseer.
- 946 Gilks, W. R., Richardson, S., & Spiegelhalter, D. (1995). *Markov chain Monte Carlo*
 947 *in practice*. Chapman and Hall/CRC.
- 948 Gouveia, W. P., & Scales, J. A. (1998). Bayesian seismic waveform inversion: Pa-
 949 rameter estimation and uncertainty analysis. *Journal of Geophysical Research:*
 950 *Solid Earth*, *103*(B2), 2759–2779.
- 951 Gregory, P. (2005). *Bayesian Logical Data Analysis for the Physical Sciences: A*
 952 *Comparative Approach with Mathematica® Support*. Cambridge University Press.
- 953 Guerri, M., Cammarano, F., & Tackley, P. J. (2016). Modelling earth’s surface
 954 topography: decomposition of the static and dynamic components. *Physics of the*
 955 *Earth and Planetary Interiors*, *261*, 172–186.
- 956 Haario, H., Laine, M., Mira, A., & Saksman, E. (2006). DRAM: efficient adaptive
 957 MCMC. *Statistics and computing*, *16*(4), 339–354.
- 958 Haario, H., Saksman, E., Tamminen, J., et al. (2001). An adaptive Metropolis algo-
 959 rithm. *Bernoulli*, *7*(2), 223–242.
- 960 Hashin, Z., & Shtrikman, S. (1962). A variational approach to the theory of the ef-
 961 fective magnetic permeability of multiphase materials. *Journal of applied Physics*,
 962 *33*(10), 3125–3131.
- 963 Hashin, Z., & Shtrikman, S. (1963). A variational approach to the theory of the
 964 elastic behaviour of multiphase materials. *Journal of the Mechanics and Physics*
 965 *of Solids*, *11*(2), 127–140.
- 966 Hassani, B., & Renaudin, A. (2013). The cascade bayesian approach for a controlled
 967 integration of internal data, external data and scenarios.
- 968 Hassani, B. K., & Renaudin, A. (2018). The cascade bayesian approach: Prior trans-
 969 formation for a controlled integration of internal data, external data and scenarios.
 970 *Risks*, *6*(2), 47.
- 971 Herrmann, R. B., & Ammon, C. J. (2002). Computer programs in seismology:
 972 Surface waves, receiver functions and crustal structure. *St. Louis University, St.*
 973 *Louis, MO*.
- 974 Hesthaven, J. S., Rozza, G., & Stamm, B. (2016). *Certified reduced basis methods for*
 975 *parametrized partial differential Equations*. Springer.
- 976 Hu, H., Dai, L., Li, H., Hui, K., & Sun, W. (2017). Influence of dehydration on the
 977 electrical conductivity of epidote and implications for high-conductivity anoma-
 978 lies in subduction zones. *Journal of Geophysical Research: Solid Earth*, *122*(4),
 979 2751–2762.
- 980 Huang, Z., Li, H., Zheng, Y., & Peng, Y. (2009). The lithosphere of north china cra-
 981 ton from surface wave tomography. *Earth and Planetary Science Letters*, *288*(1-
 982 2), 164–173.
- 983 Jackson, I., & Faul, U. H. (2010). Grainsize-sensitive viscoelastic relaxation in
 984 olivine: Towards a robust laboratory-based model for seismological application.
 985 *Physics of the Earth and Planetary Interiors*, *183*(1-2), 151–163.

- 986 Jackson, I., Fitz Gerald, J. D., Faul, U. H., & Tan, B. H. (2002). Grain-size-sensitive
987 seismic wave attenuation in polycrystalline olivine. *Journal of Geophysical Re-*
988 *search: Solid Earth*, 107(B12), ECV–5.
- 989 Jegen, M. D., Hobbs, R. W., Tarits, P., & Chave, A. (2009). Joint inversion of
990 marine magnetotelluric and gravity data incorporating seismic constraints: Pre-
991 liminary results of sub-basalt imaging off the Faroe Shelf. *Earth and Planetary*
992 *Science Letters*, 282(1-4), 47–55.
- 993 Jones, A. G., Afonso, J. C., & Fullea, J. (2017). Geochemical and geophysical
994 constrains on the dynamic topography of the Southern African Plateau. *Geochem-*
995 *istry, Geophysics, Geosystems*, 18(10), 3556–3575.
- 996 Jones, A. G., Evans, R. L., & Eaton, D. W. (2009). Velocity–conductivity rela-
997 tionships for mantle mineral assemblages in archaic cratonic lithosphere based
998 on a review of laboratory data and Hashin–Shtrikman extremal bounds. *Lithos*,
999 109(1-2), 131–143.
- 1000 Kaipio, J., & Somersalo, E. (2006). *Statistical and computational inverse problems*
1001 (Vol. 160). Springer Science & Business Media.
- 1002 Kalscheuer, T., Bastani, M., Donohue, S., Persson, L., Pfaffhuber, A. A., Reiser,
1003 F., & Ren, Z. (2013). Delineation of a quick clay zone at smørgrav, norway,
1004 with electromagnetic methods under geotechnical constraints. *Journal of Applied*
1005 *Geophysics*, 92, 121–136.
- 1006 Karato, S.-I. (1990). The role of hydrogen in the electrical conductivity of the upper
1007 mantle. *Nature*, 347(6290), 272.
- 1008 Karato, S.-i. (2006). Remote sensing of hydrogen in earth’s mantle. *Reviews in Min-*
1009 *eralogy and Geochemistry*, 62(1), 343–375.
- 1010 Karato, S.-i., & Wang, D. (2013). Electrical conductivity of minerals and rocks.
1011 *Physics and Chemistry of the Deep Earth*, 5, 145–182.
- 1012 Khan, A. (2016). On Earth’s mantle constitution and structure from joint analy-
1013 sis of geophysical and laboratory-based data: An example. *Surveys in Geophysics*,
1014 37(1), 149–189.
- 1015 Khan, A., Connolly, J., & Olsen, N. (2006). Constraining the composition and ther-
1016 mal state of the mantle beneath europe from inversion of long-period electromag-
1017 netic sounding data. *Journal of Geophysical Research: Solid Earth*, 111(B10).
- 1018 Khan, A., Connolly, J., & Taylor, S. (2008). Inversion of seismic and geodetic
1019 data for the major element chemistry and temperature of the Earth’s man-
1020 tle. *Journal of Geophysical Research: Solid Earth*, 113(B9), B09308. doi:
1021 10.1029/2007JB005239
- 1022 Lebedev, S., & Van Der Hilst, R. D. (2008). Global upper-mantle tomography with
1023 the automated multimode inversion of surface and S-wave forms. *Geophysical*
1024 *Journal International*, 173(2), 505–518.
- 1025 Liu, H.-P., Anderson, D. L., & Kanamori, H. (1976). Velocity dispersion due to
1026 anelasticity; implications for seismology and mantle composition. *Geophysical*
1027 *Journal International*, 47(1), 41–58.
- 1028 Mallick, K., & Verma, R. (1979). Time-domain electromagnetic sound-
1029 ing—computation of multi-layer response and the problem of equivalence in in-
1030 terpretation. *Geophysical Prospecting*, 27(1), 137–155.
- 1031 Manassero, M. C., Afonso, J. C., Zyserman, F., Zlotnik, S., & Fomin, I. (2020). A
1032 Reduced Order Approach for Probabilistic Inversions of 3D Magnetotelluric Data
1033 I: General Formulation. *Geophysical Journal International*, 223(3), 1837–1863.
- 1034 Matas, J., & Bukowinski, M. S. (2007). On the anelastic contribution to the temper-
1035 ature dependence of lower mantle seismic velocities. *Earth and Planetary Science*
1036 *Letters*, 259(1-2), 51–65.
- 1037 Menke, W. (2018). *Geophysical data analysis: Discrete inverse theory*. Academic
1038 press.
- 1039 Meyn, S. P., & Tweedie, R. L. (2012). *Markov chains and stochastic stability*.

- 1040 Springer Science & Business Media.
- 1041 Mira, A., et al. (2001). On Metropolis-Hastings algorithms with delayed rejection.
1042 *Metron*, 59(3-4), 231–241.
- 1043 Moorkamp, M. (2017). Integrating electromagnetic data with other geophysical
1044 observations for enhanced imaging of the earth: a tutorial and review. *Surveys in*
1045 *Geophysics*, 38(5), 935–962.
- 1046 Moorkamp, M., Fulla, J., Aster, R., & Weise, B. (2020). Inverse methods, resolu-
1047 tion and implications for the interpretation of lithospheric structure in geophysical
1048 inversions.
- 1049 Moorkamp, M., Jones, A., & Eaton, D. (2007). Joint inversion of teleseismic re-
1050 ceiver functions and magnetotelluric data using a genetic algorithm: Are seismic
1051 velocities and electrical conductivities compatible? *Geophysical Research Letters*,
1052 34(16).
- 1053 Moorkamp, M., Jones, A., & Fishwick, S. (2010). Joint inversion of receiver func-
1054 tions, surface wave dispersion, and magnetotelluric data. *Journal of Geophysical*
1055 *Research: Solid Earth*, 115(B4).
- 1056 Mosegaard, K., & Hansen, T. M. (2016). Inverse methods: Problem formulation and
1057 probabilistic solutions. *Integrated Imaging of the Earth: Theory and Applications*,
1058 *Geophysical Monograph*, 218, 9–27.
- 1059 Mosegaard, K., & Tarantola, A. (1995). Monte Carlo sampling of solutions to inverse
1060 problems. *Journal of Geophysical Research: Solid Earth*, 100(B7), 12431–12447.
- 1061 Mosegaard, K., Tarantola, A., et al. (2002). Probabilistic approach to inverse prob-
1062 lems. *International Geophysics Series*, 81(A), 237–268.
- 1063 Oldenburg, D. W. (1979). One-dimensional inversion of natural source magnetotel-
1064 luric observations. *Geophysics*, 44(7), 1218–1244.
- 1065 Omre, H. (1987). Bayesian kriging—merging observations and qualified guesses in
1066 kriging. *Mathematical Geology*, 19(1), 25–39.
- 1067 Parker, R. L. (1971). The inverse problem of electrical conductivity in the mantle.
1068 *Geophysical Journal International*, 22(2), 121–138.
- 1069 Parker, R. L. (1980). The inverse problem of electromagnetic induction: existence
1070 and construction of solutions based on incomplete data. *Journal of Geophysical*
1071 *Research: Solid Earth*, 85(B8), 4421–4428.
- 1072 Peherstorfer, B., Willcox, K., & Gunzburger, M. (2018). Survey of multifidelity
1073 methods in uncertainty propagation, inference, and optimization. *SIAM Review*,
1074 60(3), 550–591.
- 1075 Pommier, A. (2014). Interpretation of magnetotelluric results using laboratory mea-
1076 surements. *Surveys in Geophysics*, 35(1), 41–84.
- 1077 Quarteroni, A., Manzoni, A., & Negri, F. (2015). *Reduced basis methods for partial*
1078 *differential Equations: an introduction* (Vol. 92). Springer.
- 1079 Rasmussen, C. E. (1997). *Evaluation of gaussian processes and other methods for*
1080 *non-linear regression* (Unpublished doctoral dissertation). University of Toronto
1081 Toronto, Canada.
- 1082 Ray, A., & Myer, D. (2019). Bayesian geophysical inversion with trans-dimensional
1083 Gaussian process machine learning. *Geophysical Journal International*, 217(3),
1084 1706–1726.
- 1085 Rosas-Carbajal, M., Linde, N., Kalscheuer, T., & Vrugt, J. A. (2013). Two-
1086 dimensional probabilistic inversion of plane-wave electromagnetic data: methodol-
1087 ogy, model constraints and joint inversion with electrical resistivity data. *Geophys-*
1088 *ical Journal International*, 196(3), 1508–1524.
- 1089 Selway, K. (2014). On the causes of electrical conductivity anomalies in tectonically
1090 stable lithosphere. *Surveys in Geophysics*, 35(1), 219–257.
- 1091 Selway, K., & O’Donnell, J. (2019). A small, unextractable melt fraction as the
1092 cause for the low velocity zone. *Earth and Planetary Science Letters*, 517, 117–
1093 124.

- 1094 Selway, K., O'Donnell, J., & Özaydin, S. (2019). Upper mantle melt distribution
1095 from petrologically constrained magnetotellurics. *Geochemistry, Geophysics,*
1096 *Geosystems*, 20(7), 3328–3346.
- 1097 Sheen, D. (1997). Approximation of electromagnetic fields: Part I. Continuous prob-
1098 lems. *SIAM Journal on Applied Mathematics*, 57(6), 1716–1736.
- 1099 Smith, R. C. (2013). *Uncertainty quantification: theory, implementation, and appli-*
1100 *cations* (Vol. 12). Siam.
- 1101 Tarantola, A. (2005). *Inverse problem theory and methods for model parameter esti-*
1102 *mation* (Vol. 89). siam.
- 1103 Tarantola, A., & Valette, B. (1982). Inverse problems= quest for information. *Jour-*
1104 *nal of geophysics*, 50(1), 159–170.
- 1105 Vozar, J., Jones, A. G., Fulla, J., Agius, M. R., Lebedev, S., Le Pape, F., &
1106 Wei, W. (2014). Integrated geophysical-petrological modeling of lithosphere-
1107 asthenosphere boundary in central Tibet using electromagnetic and seismic data.
1108 *Geochemistry, Geophysics, Geosystems*, 15(10), 3965–3988.
- 1109 Wait, J. R. (1962). Theory of magnetotelluric fields. *J. Res. NBS D*, 66(5), 509–
1110 541.
- 1111 Wang, K., Lu, L., Maupin, V., Ding, Z., Zheng, C., & Zhong, S. (2020). Surface
1112 wave tomography of northeastern tibetan plateau using beamforming of seismic
1113 noise at a dense array. *Journal of Geophysical Research: Solid Earth*, 125(4),
1114 e2019JB018416.
- 1115 Williams, C. K., & Rasmussen, C. E. (1996). Gaussian processes for regression. In
1116 *Advances in neural information processing systems* (pp. 514–520).
- 1117 Xu, Y., Shankland, T. J., & Poe, B. T. (2000). Laboratory-based electrical con-
1118 ductivity in the Earth's mantle. *Journal of Geophysical Research: Solid Earth*,
1119 105(B12), 27865–27875.
- 1120 Yan, L., & Zhou, T. (2019). Adaptive multi-fidelity polynomial chaos approach
1121 to bayesian inference in inverse problems. *Journal of Computational Physics*, 381,
1122 110–128.
- 1123 Yang, Y., & Forsyth, D. W. (2006). Rayleigh wave phase velocities, small-scale
1124 convection, and azimuthal anisotropy beneath southern california. *Journal of Geo-*
1125 *physical Research: Solid Earth*, 111(B7).
- 1126 Yang, Y., Ritzwoller, M. H., Lin, F.-C., Moschetti, M., & Shapiro, N. M. (2008).
1127 Structure of the crust and uppermost mantle beneath the western united states
1128 revealed by ambient noise and earthquake tomography. *Journal of Geophysical*
1129 *Research: Solid Earth*, 113(B12).
- 1130 Yasar, E., & Erdogan, Y. (2004). Correlating sound velocity with the density, com-
1131 pressive strength and young's modulus of carbonate rocks. *International Journal*
1132 *of Rock Mechanics and Mining Sciences*, 41(5), 871–875.
- 1133 Yoshino, T. (2010). Laboratory electrical conductivity measurement of mantle min-
1134 erals. *Surveys in Geophysics*, 31(2), 163–206.
- 1135 Yoshino, T., Matsuzaki, T., Shatskiy, A., & Katsura, T. (2009). The effect of water
1136 on the electrical conductivity of olivine aggregates and its implications for the
1137 electrical structure of the upper mantle. *Earth and Planetary Science Letters*,
1138 288(1-2), 291–300.
- 1139 Zhang, A., Afonso, J. C., Xu, Y., Wu, S., Yang, Y., & Yang, B. (2019). The deep
1140 lithospheric structure of the junggar terrane, nw china: Implications for its origin
1141 and tectonic evolution. *Journal of Geophysical Research: Solid Earth*, 124(11),
1142 11615–11638.
- 1143 Zhang, J., & Taflanidis, A. A. (2019). Accelerating MCMC via Kriging-based adap-
1144 tive independent proposals and delayed rejection. *Computer Methods in Applied*
1145 *Mechanics and Engineering*, 355, 1124–1147.
- 1146 Zyserman, F. I., & Santos, J. E. (2000). Parallel finite element algorithm with do-
1147 main decomposition for three-dimensional magnetotelluric modelling. *Journal of*

1148 *Applied Geophysics*, 44(4), 337-351.